Phd Thesis Summary

Raman spectroscopy applied for the investigation of biological systems

By

PhD student: Alexandra Falamaş

Scientific coordinator: Prof. Dr. Vasile Chiş

Faculty of Physics, Babeş-Bolyai University
Cluj-Napoca
2012

Contents

Keywords: Raman spectroscopy, natural compounds, melanoma skin, stem cells

Chapter 1

Introduction

In this thesis, the potential of Raman spectroscopy (RS) is demonstrated for pharmaceutical and medical applications. Firstly, RS is employed for the study of chemical entities with promising pharmacological properties for skin treatments. The identification and spectroscopic characterisation of the main compounds in the outer bark of the birch trees and of their possible encapsulation methods on one side, and of dacarbazine, a currently used chemotherapeutic drug for the treatment of melanoma on the other side, are presented. Secondly, the capability of RS for analytical skin diagnosis is studied *in vivo*. Additionally, the biological activities of the natural compounds extracted from the birch tree are demonstrated in mice skin treatments. The biomolecular modifications associated with various skin pathologies are identified and the skin pharmaceutical treatment is monitored. Moreover, the Raman enhancement of biological tissues is probed using Ag colloidal nanoparticles. The aim of this study was to implement the use of surface enhanced Raman spectroscopy (SERS) for tissue pathology diagnosis. Thirdly, Raman microspectroscopy was applied for the biochemical imaging of human embryonic stem cells (hESCSs) and their fibroblasts derived progenies. The main aim was to provide a label-free noninvasive characterisation of the differentiation process and to identify and observe the distribution of the cell specific biomarkers.

The first chapter presents an overview of the biological research background, as well as a state of the art of the techniques used in pharmaceutical and the biomedical fields, focusing especially on Raman spectroscopy. The second chapter introduces the theoretical background of the experimental techniques. The theory of Raman scattering is explained in detail and the Raman spectroscopic techniques suitable for pharmaceutical and biomedical applications are presented. Additionally, the theoretical background of surface enhanced Raman, infrared and ultraviolet and visible spectroscopy are introduced. Finally, the theory behind computational chemistry methods is detailed.

Chapter three presents vibrational spectroscopic studies of natural derived compounds, coupled to density functional theory calculations. Due to the increase in cancer incidence, the need for analytical methods to determine anticancer drugs is extremely important. The natural products, a major source for new chemotherapy drugs, have been exploited here by investigating birch trees derived compounds with promising biological activities. The aim of this study was to follow the first steps involved in the process of new drugs development by employing current state of art techniques, such as Raman spectroscopy and computational methods. This implied the identification and characterisation of the active ingredients in their natural source. A complete vibrational characterisation of betulin, main pentacyclic triterpene found in the bark of the birch tree is presented for the first time. Additionally, attempts at improving its solubility were pursued by proposing and spectroscopically investigating two encapsulation methods.

Chapter four continues the pharmaceutical applications of vibrational spectroscopic methods, focused this time on the characterisation of dacarbazine, a chemotherapeutic drug, using Raman, infrared, and surface enhanced Raman spectroscopies. A Raman pH study was performed to identify additional species of the drug, sensitive to the pH modification of the environment. SERS studies are additionally introduced for detecting minimal concentrations of the drug by amplifying the vibrational modes of the molecules attached to or in close vicinity to the metal nanostructures. The functional groups involved in the

adsorption and the adsorbate orientation to the metal surface are proposed based on the SERS selection rules.

Melanoma is an aggressive type of skin cancer, which could be treated if identified in the initial phase. The most widely used method for the characterisation of suspicious lesion is the histopathologic examination. This is however, an invasive technique whose diagnosis exactitude is subjected to the examiner's interpretation. The motivation for the study presented in chapter four of this thesis was based on the recent applications of vibrational spectroscopic methods for disease diagnosis and characterisation of biological samples. The *in vivo* ability of Raman microspectroscopy is probed for the characterisation of mice skin in specimens with various pathologies induced in the laboratory in chapter five of this thesis. Two important questions are to be answered here, whether Raman microspectroscopy can successfully differentiate between the various skin pathologies and monitor the applied treatment, and whether the pharmaceutical formulations based on the active ingredients in the natural compounds investigated in the first part of the thesis show any beneficial activities on the chemically treated mice skin.

Raman scattering is however, a weak effect, which is additionally overlapped by the auto-fluorescence signal of biological tissues. Surface enhanced Raman spectroscopy (SERS) can overcome these problems due to the amplified Raman signal observed in the presence of metallic nanoparticles. The multitude medical applications of SERS spectroscopy has motivated us to probe the ability of silver colloidal nanoparticles penetrated into biological tissues for enhancing the weak Raman scattering and molecular characterisation of the samples. Here, SERS effect is employed for both *in vivo* and *ex vivo* applications in biological skin tissues. A SERS characterisation of the mouse skin samples is provided, as well as an attempt to elucidate the SERS mechanism resulted from the biological samples. Additionally, the development of cresyl violet SERS labels is presented and their capacity for sensitive local chemical probing of native biological molecules in mouse skin tissues is probed.

Chapter six focuses on label-free Raman microspectroscopy studies based on identifying and monitoring the intracellular distribution of biomolecular markers specific to the differentiation process in human embryonic stem cells (hESCs) and their fibroblasts derived progenies. The current need for non-invasive techniques for the characterisation of the differentiation process in stem cells can be met by Raman spectroscopy, which is able probe the biochemical content of cells in a label-free, non-destructive manner. Thus, the nucleic acids differentiation process characteristic Raman biomarkers are identified and their distribution is monitored inside the cells. Furthermore, fluorescence imaging is employed to support and potentiate the Raman results. Additionally, a spectral fitting model is proposed for the decomposition of individual Raman spectra and evaluation of the local intracellular biomolecular composition. The aim of this procedure is to identify site-specific contributions of proteins and nucleic acids in the cells.

The work is summarised in chapter seven of this thesis. Moreover, possible future work directions are set.

Chapter 2

Vibrational characterisation of pharmacologically natural compounds

2.1 Introduction

In the frames of modern medicine, natural compounds have showed their importance as a source of bioactive compounds in different therapeutic areas [1, 2]. The birch bark has been the subject of respect and admiration throughout prehistory and history, as well as the subject of scientific research and industry in the modern world [3, 4]. The outer bark of birch tree is rich in pentacyclic triterpenes components, such as betulin, betulinic acid, lupeol, betulin 3-caffeate, and other minor components [5,6]. Despite some disadvantages which may inhibit their candidatures as future drugs, such as low water solubility or high molecular weight, the National Cancer Institute (NCI) is assisting studies based on the development of topical formulations based on betulinic acid for potential clinical trials [7]. Betulin (lup-20(29)-ene-3β,28-diol) is found in the outer layers of the birch bark and it is responsible for its white color. It presents a broad field of biological properties, e.g. anti-cancer, anti-bacterial, anti-inflammatory, anti-fungal, and anti-viral [8–12].

The promising biological activities of triterpenes and the extensive latest research on this subject, led us towards initiating a research project (`http://phys.ubbcluj.ro/cercetare/granturi/pinzaru/english/index_en.htm`) established on formulating medications based on natural compounds extracted from the bark of the birch tree, with the aim of applying them in rodents skin treatments. The process of drug discovery from plants is a complex process involving several steps such as the plant collection, the preparation of the plants extracts, the bio-assay of the extracts, and the isolation and structure elucidation of the active components, followed by toxicity, delivery and activity studies. In this manner, natural extracts samples were obtained from birch bark collected from Romanian forests and spectroscopic investigations were conducted with the aim of characterising them and identifying the main components. This sets up the first two hypothesis of this study, which are: the main components in the birch bark and the natural extracts can be identified using FT-Raman spectroscopy and a complete vibrational characterisation of the main active ingredient in the birch bark can be carried through based on experimental and theoretical data.

While attempting to devise ointments and other pharmaceutical compounds based on triterpenes, the main encountered difficulty was their low solubility. Recent literature suggests that this can be solved through cyclodextrin (CD) complexation and several studies of inclusion complexes (see Fig. 2.1) between triterpenes and cyclodextrins have been conducted [13–16]. Due to the CD complexation, the drug will dissolve faster, will attain a higher solubility, and it will result in a more complete absorption [17]. The third and final hypothesis of this study is thus to propose pentacyclic triterpenes solubility increasing methods and provide a vibrational characterisation of the resulted compounds. Addionally, nanoemulsions were also prepared in association with the Department of Toxicology at the Faculty of Pharmacy,

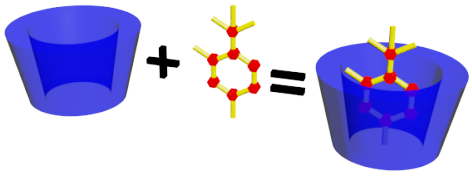

Figure 2.1: Schematic representation of the cyclodextrin molecular encapsulation.

University of Medicine and Pharmacy in Timisoara, Romania and the Department of Pharmaceutical Sciences at the Northeastern University in Boston, Massachusetts, USA, as an alternative method for improving the solubility of the triterpenes. Nanoemulsions are dispersions of oil and water [18, 20, 21] widely known for their investigations as drug carriers [18, 19].

2.2 Results and discussions

2.2.1 FT-Raman investigations of the birch bark and the natural extracts

The natural extracts

Six natural extract samples were obtained from the outer part of birch bark, plant material harvested from the Aninei Mountains (Banat region, Southwest of Romania). FT-Raman spectra were recorded from each sample and are presented in Fig. 2.2. The highest intensity Raman signal with well resolved vibrational bands were exhibited by the precipitates, which appeared as cream colored solutions with white crystals.

The main triterpenes

In order to identify and differentiate between the components found in the natural extracts, FT-Raman spectra of the main known triterpenes found in the outer bark of the birch tree were recorded and presented in Fig. 2.3 in comparison to an FT-Raman spectrum of a natural extract. Raman features corresponding to the structural-functional groups of each of the main pentacyclic triterpenes were identified. The vibrational characterization of the active Raman bands indicate that betulin is the main triterpene found in the natural extracts, although other lower quantities compounds can also be present. Following the identification of the main component in the natural extracts, a spectroscopic characterisation of the birch bark was employed. The aim of this study was to investigate the composition of the raw birch bark. Fig. 2.3 presents the FT-Raman spectrum of the bark (spectrum g) in comparison to the FT-Raman spectra of the main triterpenes and the natural extract. Raman fingerprint bands characteristic to all of the previously analysed triterpenes were identified in the raw birch bark, among other impurities. These results are successful in demonstrating the amazing selectivity of the FT-Raman technique for identifying the active species from their natural source.

2.2.2 Vibrational characterisation of betulin

Since the previous results identified betulin as the main compound in the outer bark of the birch tree, the next aim of this study is to provide a complete vibrational characterization of this compound. The

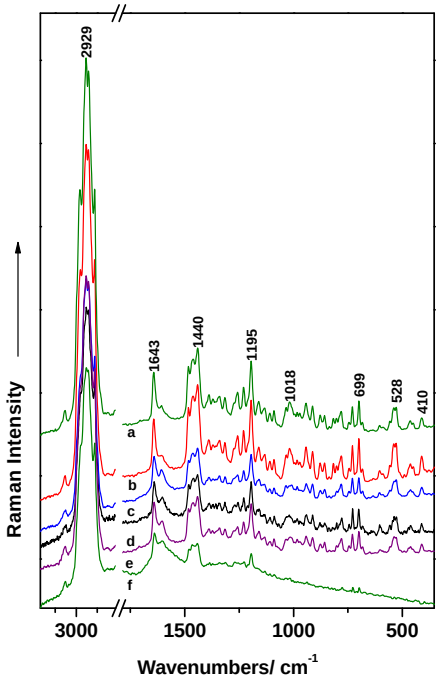

Figure 2.2: FT-Raman spectra of the natural extract samples (the code of the samples are shown to the left).

investigation was carried out by employing FT-Raman and FT-IR spectroscopy techniques, as well as DFT quantum chemical calculations.

Geometry optimisation

The optimised geometry of betulin obtained at the B3LYP/6-31 G(d) level of theory is shown in Fig.2.4. Betulin ($C_{30}H_{50}O_2$) is a triterpene comprising four six-member rings and one five-member ring. It is important to notice the primary hydroxyl group in the C28 position, the secondary hydroxyl group in the C14 position and the alkene moiety in the C75 position. Chemical modifications can be easily performed at these positions to produce derivatives for structure-activity relationship studies [8]. For example, betulinic acid can be obtained through modifications at the C28 position and changing the CH_2OH group into C=O-H-O.

Vibrational spectra analysis

Experimental and theoretical FT-IR and FT-Raman spectra of betulin are shown in Fig. 2.5. The computed vibrational wavenumbers, their IR intensities, and Raman activities were employed to identify the vibrational modes explicitly. The main fingerprint FT-IR and FT-Raman bands, the calculated scaled wavenumbers, as well as the detailed vibrational assignments of the fundamental modes of betulin are presented in Table 2.1.

The dominant bands observed in the FT-IR spectrum are measured at 1643, 1450, 1373, 1006, 876 cm^{-1}. The 1643 cm^{-1} band is assigned to a complex contribution of the C=C stretching and CH_2 bending vibrations in the terminal methyl group. Most of the bands in this spectral range are assigned to rocking and bending vibrations of the OH, CH, CH_2 and CH_3 groups as well as skeletal bending modes (Table 2.1). The 1450 cm^{-1} band is assigned to CH_3 and CH_2 bending vibrations, the 1373 cm^{-1} band is assigned

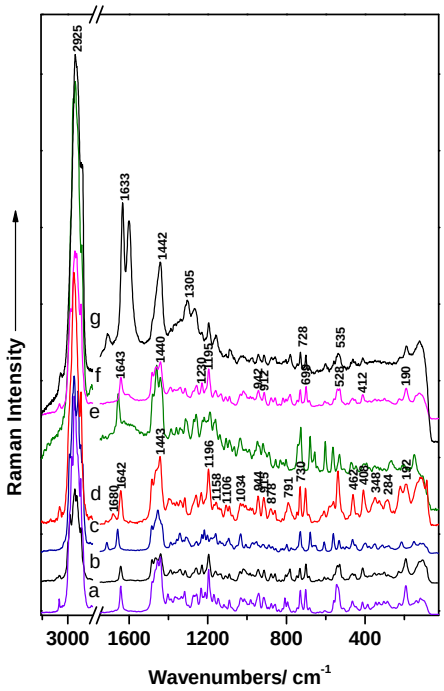

Figure 2.3: FT-Raman spectra of (a) lupeol, (b) betulin, (c) ursolic acid, (d) betulinic acid, (e) oleanolic acid, (f) the natural extract and (g) raw bark of the birch tree.

to umbrella mode of the CH_3 groups in the second, third and fourth rings of the molecule. The 1006 and 984 cm^{-1} bands correspond mainly to stretching, rocking and bending vibrations in the CH_2CH_3 group. Another intense band seen in the FT-IR spectrum of betulin is the 876 cm^{-1} assigned to wagging vibrations of the CH_2 group in the alkene moiety.

In the high wavenumber region a complex shaped band centered at 2927 cm^{-1} has been observed, while in the fingerprint region the FT-Raman spectrum presents complex shaped bands at 1643, 1484, 1464, 1440, 1195, 701, 530, 411, and 191 cm^{-1} characteristic for the lupane skeleton of the pentacyclic triterpene. The group of intense bands at 1484, 1464, and 1440 cm^{-1} is assigned to CH_2 and CH_3 bending vibrations. The 1195 cm^{-1} band appears due to OH bending and CH_2 twisting vibrations. The intense band at 701 cm^{-1} is assigned to twisting vibrations in the terminal group. The 411 cm^{-1} band appears due to rocking vibrations of the CH_2OH group and C-C and CH_2 and CH_3 wagging vibrations.

Table 2.1: Selective calculated vibrational wavenumbers, measured IR and Raman band positions, and assignments of betulin at B3LYP level of theory

Nr	Wavenumber			
	Theoretical	Experimental		Vibrational assignment
	ν scaled (cm^{-1})	IR	Raman	
4	191.64		228 sh	$\tau(CH_3) + \rho(CH_2OH)$
11	411.47		411 s	$\omega(CH_3) + \omega(CH_2) + \rho(CH_2) + \rho(CH_2OH)$
17	526.75		530 s	$\rho(CH_2) + \delta(C–C)$

Table 2.1: Continued

Nr	ν scaled (cm^{-1})	IR	Raman	Vibrational assignment
25	701.91		701 s	τ(H77–C76–H78)
53	1179.36		1195 s	$\delta(OH) + \tau(CH_2)$
69	1458.5		1440 s	$\delta(CH_3)R1 + \delta(CH_2)R1, R2, R4.R5$
72	1485.39		1464 s	$\delta(CH_3) + \delta$(H17–C15–H18) $+ \delta(CH_2)R3$
73	1499.06	1485 sh	1484 s	$\delta(CH_3)R1, R2, R3 + \delta(CH_2)R1, R3$
74	1663.73	1639 m	1645 s	$\delta(CH_2) + \nu$(C=C) alkene $+ \delta$(CH)R5
80	2970.29		2927 vvs	$\nu(CH_3)R2, R3, R4 + \nu_{as}(CH_2)R1, R3$
87		3362 s	3358 vw	ν(O71–H72)
88	3612.62	3465 s	3437 vvw	ν(O73–H74)

Abbreviations: δ - bending, ν - stretching, ω - wagging, τ - twisting, ρ - rocking, vw - very weak, w - weak, m - medium, s - strong, vs - very strong, sh- shoulder.

2.2.3 Spectroscopic investigations of birch bark active substances encapsulation methods

Experimental and theoretical studies of betulin-cyclodextrin guest-host type complexes

Due to betulin's recent found biomedical activities [8,22,23], a special attention was paid to the possibility of creating betulin based pharmaceutical formulations. However, the poor solubility of the molecule hampers the formulation, thus solubility enhancing methods need to be addressed. Two different methods of encapsulation are presented here and the resulted products are investigated using experimental and theoretical spectroscopic techniques.

The first one proposes the inclusion of the active substance into cyclodextrins, torus-like molecules capable of incorporating foreign molecules into their cavities [16, 24], which should improve the drug's solubility and bioavailability [25]. The cyclodextrins of choice used in this study are the hydroxyl-propyl-gamma-cyclodextrins (HPGCD). 1:1 and 1:2 inclusion complexes were formulated using betulin and betulinic acid as "guest" molecules. In order to investigate the structure-function relationship between betulin and HPGCD, first, the molecules were subjected to quantum chemical calculations. Foremost, an optimisation calculus on the separate molecules, followed by the 1:1 inclusion complex was performed using AM1 level of theory. The optimised geometries are presented in Fig. 2.6.

The theoretical calculations were conducted on the γ-CD and the betulin molecule previously investigated. The cyclodextrin moleculeis built of eight glucose units. After optimising the geometries for the separate molecules, the betulin molecule was placed inside the cyclodextrin cavity and a full optimisation was performed on this complex. To elucidate how the two molecules interact with each other, the inclusion complex and the separate molecules were further subjected to a frequency calculus as well as FT-Raman spectroscopy.

The betulin-cyclodextrin inclusion complexes

The ability of the FT-Raman technique is probed for identifying fingerprint bands characteristic to each of the compounds present in a mixture. Fig. 2.7 presents the FT-Raman spectra of betulin, 1:1 and 1:2 inclusion complexes, and HPGCD, and the theoretical AM1 Raman spectrum of the 1:1 inclusion complex betulin-γCD. The Raman spectra of the inclusion complexes exhibit the main characteristic features of HPGCD and to some extent additional contributions from the guest specie. The FT-Raman spectrum of

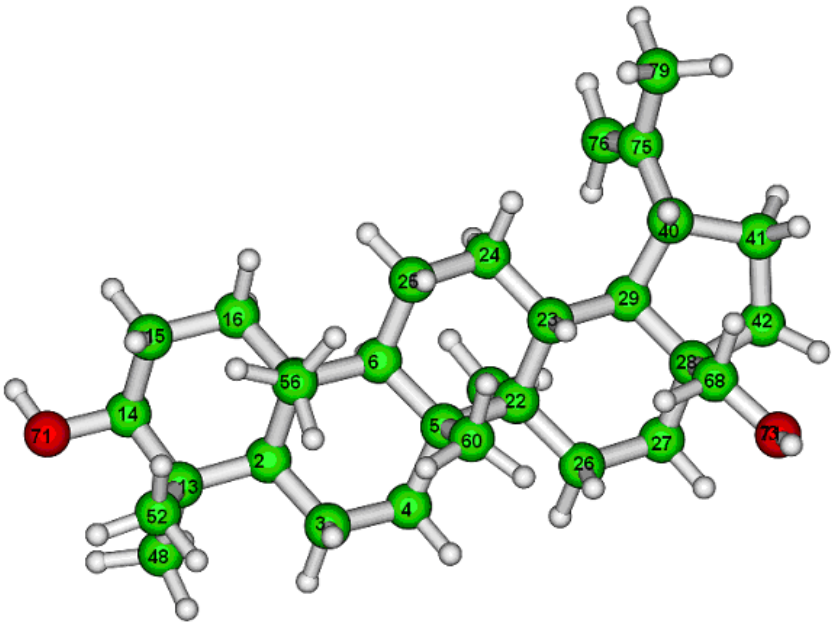

Figure 2.4: The B3LYP/6-31 G(d) optimised geometry of betulin.

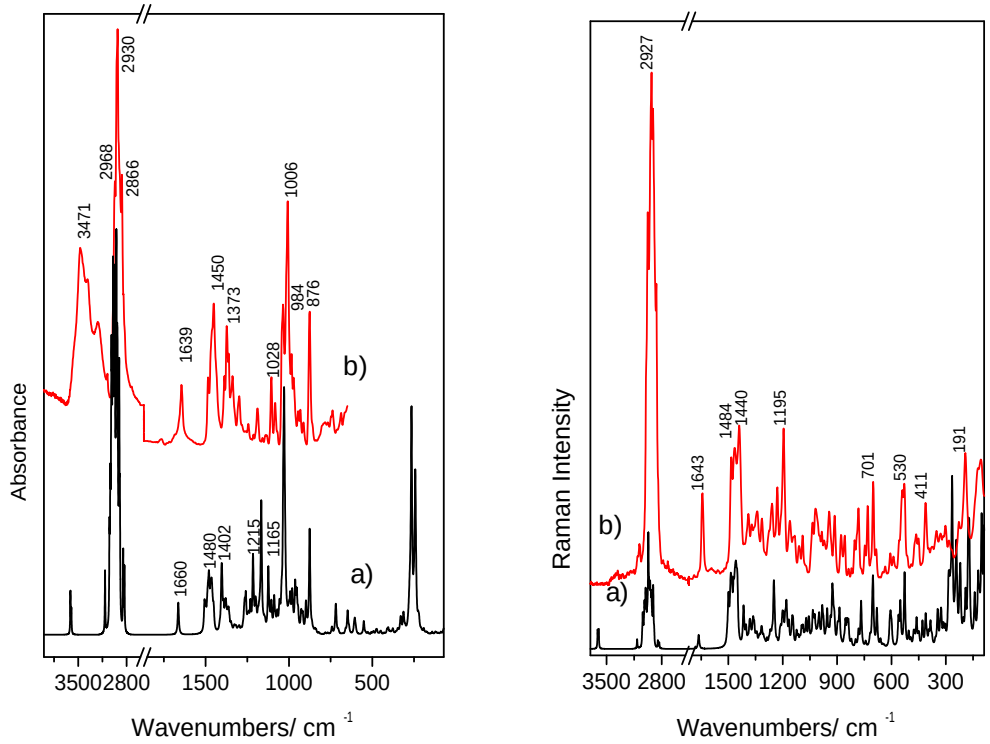

Figure 2.5: Theoretical (a) and experimental (b) FT-IR (left) and FT-Raman (right) spectra of betulin.

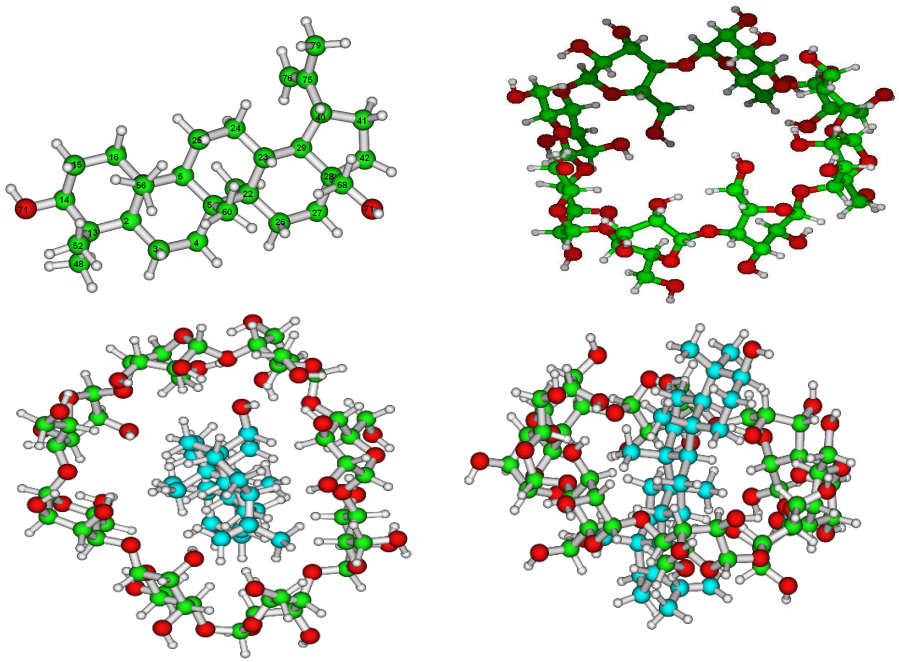

Figure 2.6: The AM1 optimised geometries of betulin (upper left), gamma-cyclodextrin (upper right) and of the 1:1 kneading product inclusion complex of the two molecules seen from different perspectives (bottom).

the 1:1 inclusion complex resembles well the sum of the individual spectra of the guest and host molecules. Moreover, one can notice the absence of the HPGCD characteristic Raman bands in the following spectral ranges: 150–200, 400–550, 700–750, 1190–1250, and 1400–1500, and 1645 cm^{-1}. To evidence the changes caused by the guest-host interaction, further investigations of these spectral regions were carried through.

The vibrational analysis suggests the existence of a weak interaction between betulin and the cyclodextrin. The broadening, decrease in intensity, and shifts in wavenumbers of the betulin characteristic vibrational modes which are clearly visible in the FT-Raman spectra of the inclusion complexes, confirm the interaction between the two species. The spectrum of the 1:1 inclusion complex showed broadening of the 1229, 1195, and 192 cm^{-1} bands, with the 1229 cm^{-1} band exhibiting the highest increase of the FWHM. Both 1195 and 1229 cm^{-1} bands are assigned to CH and OH bending vibrations in both hydroxy groups of the betulin. The AM1 calculated spectrum of the 1:1 inclusion complex shows the most intense band in the spectrum at 1195 cm^{-1} band at 1177 cm^{-1} and is attributed to CH bending vibrations and OH bending vibrations in the C28 position of betulin and CH and OH bending vibrations of the cyclodextrin. These results suggest that the CH_2OH group of betulin forms hydrogen bonds with the HPGCD cavity in the case of the 1:1 inclusion complex. In the case of the 1:2 inclusion complex, the 1645 cm^{-1} band, assigned to CH_2 bending vibrations and C=C stretching vibrations in the alkene moiety terminal group of betulin, presents a broadening of the FWHM from 11.42 (pure betulin) to 14.02 cm^{-1} and a decrease in intensity. The increase of the bandwidths, suggests the decrease of the vibrational relaxation time and confirms the formation of the inclusion complex [26]. These observation suggest the formation of the inclusion complex through interactions between the CH_2 group in the alkene moiety terminal of betulin and the CD cavity.

Nanoemulsion formulation and FT-Raman characterisation

The second encapsulation method proposed for increasing the solubility of betulin is its formulation in flax-seed oil containing nanoemulsion [20]. The transmission electron microscopy (TEM) images shows

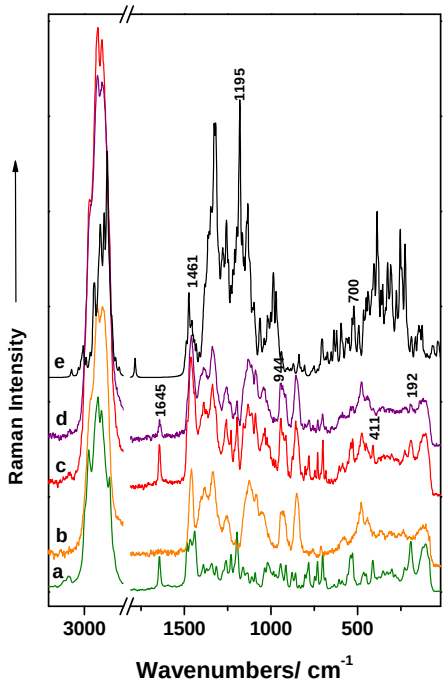

Figure 2.7: FT- Raman spectra of betulin (a), HPGCD (b), 1:1 complex (c), 1:2 complex (d), and the AM1 calculated Raman spectrum of the 1:1 inclusion complex (e).

that the nanoemulsion is composed of spherical droplets with uniform distribution (Fig. 2.8 left), with ane average diameter of 200 nm.

For a complete characterisation of the blank and betulin containing nanoemulsion, FT-Raman spectroscopy was also employed. The aim of this was to probe the capacity of the Raman spectroscopy in evidencing spectral characteristics of the nanoemulsions, as well as in identifying betulin, the active specie. Fig. 2.8right presents the FT-Raman spectra of betulin powder (a) in comparison to that of the nanoemulsion formulation (b) and the blank emulsion (c). The FT-Raman signal of both nanoemulsions is dominated by the characteristic Raman bands of the flax seed oil (not shown here). The overlapping of the nanoemulsion Raman bands with those characteristic to betulin hamper its monitoring in the nanoemulsion formulation using conventional Raman spectroscopy. The only differences seen between the Raman spectra of the two emulsions is the slight shifting towards smaller wavenumbers of some of the betulin containing nanoemulsion Raman bands (447, 1745 and 3216 cm^{-1}) when compared to the corresponding ones in the blank emulsion spectrum. Keeping in mind the encapsulation efficiency result of betulin in the oil droplets, as well as the unfortunate overlapping of the betulin fingerprint bands with those of the flax seed oil, we can conclude that the FT-Raman technique could not be used for monitoring the active specimen in the nanoemulsion. However, a vibrational characterisation was possible and the FT-Raman technique evidenced the oil phase the emulsion.

2.3 Conclusions

This study presents the spectroscopic investigations of natural compounds present in the birch bark with the aim of identifying and characterising the main active ingredients. This investigation is of great importance when formulating pharmaceutical compounds based on these molecular entities, as well as for identifying them in different media.

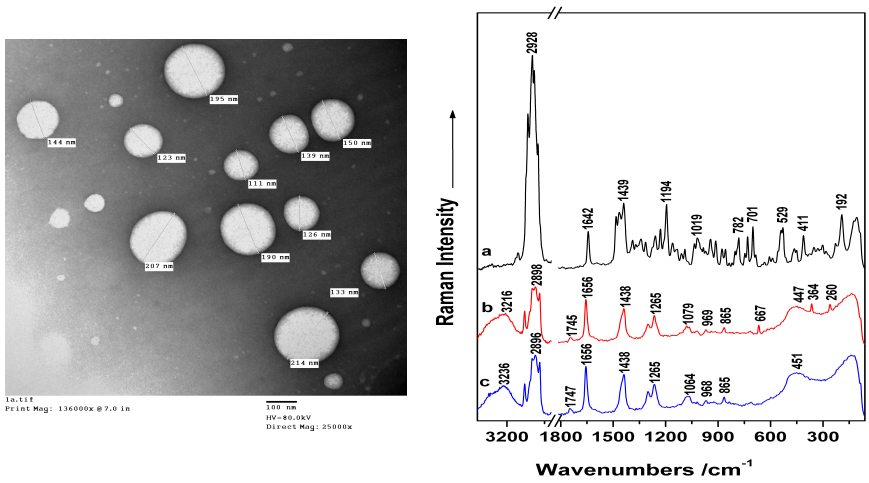

Figure 2.8: (left) Transmission electron microscopy analysis of betulin-containing nanoemulsion and (right) FT-Raman spectrum of betulin (a) in comparison to those of the betulin based nanoemulsion (b) and of the blank nanoemulsion (c).

The bulk was characterised using FT-Raman spectroscopy and it was shown that the components of the birch bark extracts can be recognised and differentiated by vibrational spectroscopy. Additionally, betulin was found to be the main pentacyclic triterpene in the outer bark and in the natural extracts. A complete vibrational characterisation of betulin was achieved, based on both experimental and theoretical data. The wavenumber position and vibrational assignment of the main bands of the characteristic functional groups of the betulin molecule were given and discussed. The investigation presented here showed that there is an excellent agreement between the calculated frequencies and the experimental ones, thus indicating that the theoretical model was well computed.

The second part of the chapter focused on proposing solubility increasing methods and their characterisation through vibrational spectroscopic methods. The first investigation presented the characterisation of betulin-cyclodextrin guest-host type complexes. The vibrational characterization is based on the FT-Raman spectroscopic data and the quantum chemical calculations employed for the characterisation of the two molecules, as well as their inclusion complexes. In the case of the 1:1 inclusion complex, the vibrational analysis revealed the existence of interactions between the CH_2OH group of the betulin and the cavity of the HPGCD molecule. The alkene moiety terminal group of betulin is left out of the cyclodextrin cavity, available for other interactions. When preparing the 1:2 inclusion complex of betulin and two HPGCD molecules, the situation differs slightly. The spectrum of the 1:2 inclusion complex is dominated by spectral features of cyclodextrins, while the spectral features of betulin are decreased in their relative intensities. Among these, the formation of hydrogen bonds is suggested by the broadening and shifting of betulin bands characteristic to both the CH_2OH and alkene moiety groups. This may suggest that the cyclodextrins surround the betulin molecule in an attempt to form the guest-host complex.

A second alternative to inclusion complexes is proposed, using nanoemulsions based on betulin. The betulin molecules can be incorporated in nanometer sized oil droplets which help to deliver the active substance to the target. An FT-Raman characterisation of the nanoemulsion formulation was probed, however, the technique was unsuccessful in identifying betulin in the oil phase which dominated the vibrational spectrum.

Chapter 3

Vibrational characterisation of dacarbazine anti-cancer chemotherapy drug

3.1 Introduction

Dacarbazine,(5-(3,3-dimethyltriazeno)imidazol-4-carboxamide) (DTIC) is an active agent for treating malignant melanoma approved by the US Food and Drug Administration. DTIC, first synthesised in 1959, is a light-sensitive compound approved for the treatment of metastatic melanoma and other skin diseases [29]. Dacarbazine is employed as a single agent for the treatment of melanoma and in combination with other drugs for soft tissue sarcomas [30]. A phase III randomised trial investigating stage IV melanoma concluded that the response rate of the tumor to dacarbazine was 10.2%, consistent with other published data, and the median survival time was of 6.4 months [31]. Numerous studies have been conducted over the years in order to test the toxicity and chemotherapeutic activity of dacarbazine against cell cultures or to develop new methods for preparation of dacarbazine based formulations [32–34]. Some of these studies blame its anti-cancer activity, while others find it active against some cell types, or suggest its use in combination with other drugs.

Regardless of its inclusion in phase trials, dacarbazine is still submitted to preclinical development studies of its physicochemical and biopharmaceutical properties, proving that there are still many unknown facts related to this compound. LC-MS and LC-UV studies were conducted to test its stability and compatibility with different materials [35, 36], and LC-MS/MS studies were carried out for the determination of DTIC and AIC its final metabolite in blood plasma [37]. Dacarbazine was found to be unstable in solutions and to rapidly photo-decompose. As a conclusion, a usual dose of 800 ng/m^2 dacarbazine solution could deliver a dose of 60.2 mg/m^2 of 2-azahypoxanthine, the main degradation product which was considered the main cause for the appearance of adverse effects. The protection of dacarbazine from light and reduction of its degradation lead to an inhibition of the side effects [38]. These studies support the belief that despite its use in clinical trials, there are still many unknown factors related to its properties and mechanism of action. Due to the biomedical importance of the dacarbazine molecule, the aim of this study is to elucidate more facts related to the molecule's physical and chemical properties by employing vibrational spectroscopic and computational chemistry methods.

3.2 Results and discussions

3.2.1 Geometry optimization

The structure of DTIC is composed of a carboxamide group (C=O-NH_2), an imidazole ring ($C_3H_4N_2$), a triazene chain (N_3H_3), and two methyl groups (Fig. 3.1). The imidazole ring exists in two tautomeric forms, since each of the nitrogens in the ring can be protonated. The minimum energy conformation, resulted following a potential energy scan, was optimized at the B3LYP/6-31 G(d) level of theory and further checked for imaginary frequencies by performing a vibrational analysis.

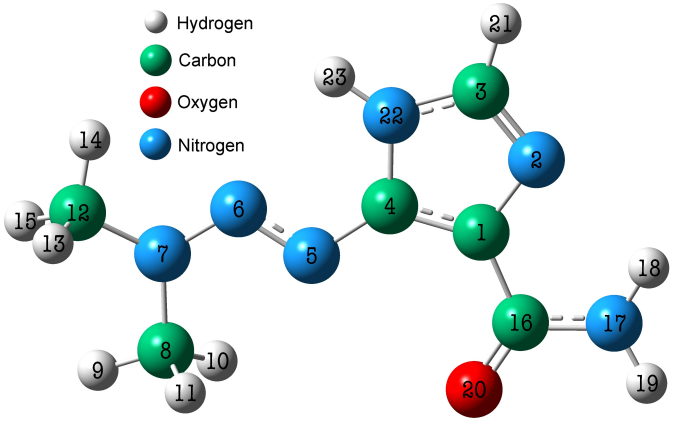

Figure 3.1: B3LYP/6-31 G(d) optimised molecular structure of the global minimum energy conformation and atom numbering scheme of DTIC.

3.2.2 Raman spectra of dacarbazine at different pH values

Raman spectroscopy was employed here for evidencing the protonation and deprotonation species of dacarbazine in saturated aqueous solutions (Fig. 3.2). For a proper assignment of the experimentally observed Raman bands, DFT calculations were employed in vacuum at the B3LYP/6-31++ G(d,p) level of theory, which gave very good results especially for the deprotonated specie due to the added diffuse functions.

Three dacarbazine species were detected, as it follows: below pH 3, the Raman spectra indicate the presence of the protonated form of dacarbazine. The protonated specie of the DTIC molecule is indicated by the intense band centered at 1343 cm^{-1} which among other vibrations includes bending vibrations of the NH protonated site (Fig. 3.3a). Other fingerprint bands are measured at 1470 cm^{-1} attributed to NH bending at the N3 protonation site coupled to CH_3 bending vibrations, 1514 cm^{-1} assigned to CH and NH bending vibrations, and the 1621 cm^{-1} assigned to NH_2 and NH bending at the protonation site in the imidazole ring and C-C stretching vibrations.

At pH 4, both protonated and neutral forms can be detected, and the neutral form becomes prominent when increasing the pH. The 1343 cm^{-1} band decreases in intensity, while the 1364 cm^{-1} shoulder is shifted to 1375 cm^{-1} and increases in intensity, becoming very strong at higher pH values. This band is assigned to N-N stretching vibrations coupled to CH_3 umbrella and NH bending vibrations at the N23 site. New bands characteristic to the neutral form present in the pH range 4 to 11 are the 1410, 1445, and 1489 cm^{-1} bands assigned mainly to CH_3 bending vibrations, 1548 cm^{-1} assigned to NH_2 bending vibrations, evidencing the presence of the neutral form, and 1589 cm^{-1} assigned to NH_2 bending vibrations coupled to weaker NH bending and C-C stretching vibrations.

At pH 12 and 13, both neutral and deprotonated forms of DTIC coexist. Increasing the pH to 14, the deprotonated form of the DTIC molecule is predominant and the characteristic Raman spectrum is obtained. A new strong band can be seen at 1501 cm^{-1} assigned to CH_3 bending and N-N stretching

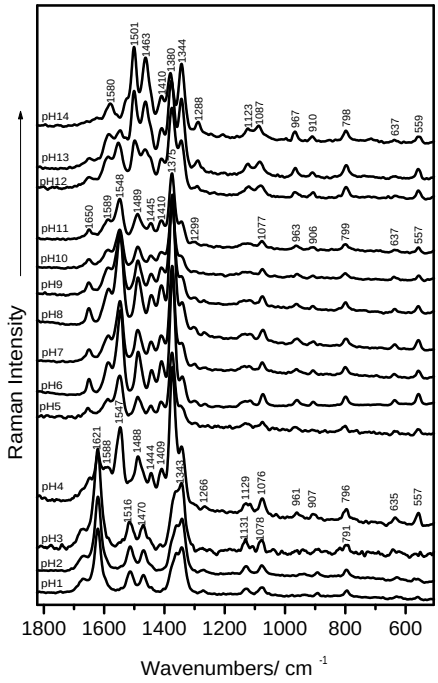

Figure 3.2: Raman spectra of the 1M dacarbazine aqueous solution recorded at different pH values. Excitation 633 nm.

vibrations. The intense new band at 1463 cm^{-1} corresponds to CH_3 bending coupled to weaker C-C stretching and NH_2 bending vibrations. The presence of the deprotonated form is indicated by the two intense bands at 1380 and 1344 cm^{-1} assigned to N-N stretching coupled to CH_3 umbrella vibrations, and CH bending coupled to C-N stretching and weak CH_3 wagging vibrations, respectively.

3.2.3 SERS spectra of dacarbazine at different pH values

Complementary to Raman, SERS spectroscopy can monitor the molecules adsorbed to or in the close vicinity of the metal surface, providing an enhanced Raman signal due to the plasmonic resonances occurring at the surface of the metals. It is well established that SERS spectroscopy can be used for the determination of adsorption sites and the orientation of molecules, as a function of the concentration on the metal surfaces and even of the pH value [39,40]. Here, SERS effect was employed for the identification of the adsorption mechanism of the DTIC species on Ag colloid (Fig. 3.4).

The adsorption of the protonated species to the silver nanosurface is detected at strong acidic conditions. Increasing the pH to 4, the adsorption of both protonated and neutral species of DTIC to the silver nanosurface can be observed, while at pH 6 only the neutral species are adsorbed to the silver surface. The adsorption of the deprotonated species is detected above pH 12. Based on the SERS spectra and the molecular electrostatic potential (MEP) calculated to aid in the interpretation and prediction of the reactive sites of dacarbazine, a chemisorption of the DTIC is proposed through the NH_2 group, in a possible tilted orientation, with the CH_3 groups close to the metal surface.

Table 3.1: Vibrational assignment of selective Raman and IR modes of dacarbazine

B3LYP/6-31 G(d) In vacuum	B3LYP/6-31 G(d) Water solvent	B3LYP/6-31++ G(d) In vacuum	FT-IR	FT-Raman	Raman pH 2	Raman pH 7	Raman pH 14	Assignment
3138	3113		3150 m	3135 w				ν(CH)
2927	2939			2928 w				$\nu_s(CH_3)$
1543	1538	1535		1545 vs		1548 s	1526 sh	$\delta(NH_2)$
1490	1482	1478	1472 m	1488 s		1489 m	1501 s	$\delta(CH_3)$
1459	1444	1448		1444 m		1445 w		$\delta(CH_3)$+ ν(N-N)
1390	1376	1385	1399 s	1372 vvs	1364 sh	1375 s	1380 s	ν(NN) +u(CH_3) +δ(NH)
1346	1350	1343	1337 m	1341 m	1343 s	1344 sh	1344 s	ν(CN)+ δ(N-N-N)+ $\delta(CH_3)$ + δ(NH)

Abbreviations: δ - bending, ν - stretching, ω - - wagging, τ - twisting, ρ - rocking, vw - very weak, w - weak, m - medium, s - strong, vs - very strong, sh- shoulder.

3.3 Conclusions

This study presents a complete vibrational assignment of dacarbazine modes, a chemotherapeutic anti-cancer drug currently used in the treatment of melanoma. The vibrational assignment is based on both Raman and IR experimental and DFT theoretical data. The fingerprint Raman bands of the chemical groups of dacarbazine molecule are identified and discussed. The modifications of the molecular structure of dacarbazine in different acid and basic aqueous media were evidenced by Raman spectroscopy. Three species of DTIC were found: the protonated form at the imidazole ring was presented at acid pH values, the neutral specie was identified in the 6-10 pH range, and at basic pH values the deprotonated form was found to be prominent.

The presence of dacarbazine molecular species attached to the silver nanoparticles was detected and their adsorption was elucidated. It was concluded that the protonated DTIC specie is adsorbed through the NH_2 group tilted to the silver surface, possibly with the free nitrogen atom in the imidazole ring closer to the metal. A similar adsorption mechanism is prosed for the neutral and protonated species as well. In these cases the CH_3 group of the molecules should be in the close vicinity of the silver nanosurface.

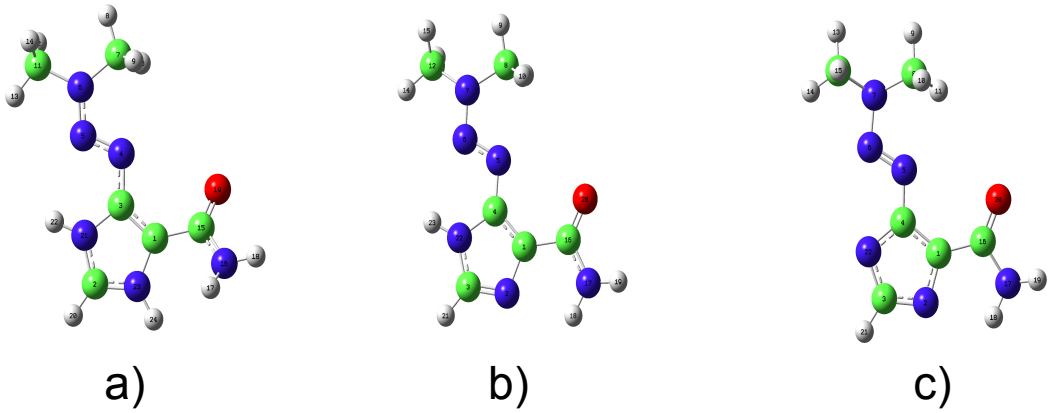

Figure 3.3: Optimised geometrical structures of the protonated (left), neutral (middle) and deprotonated (right) species of dacarbazine at the B3LYP/6-31++ G(d,p) level of theory.

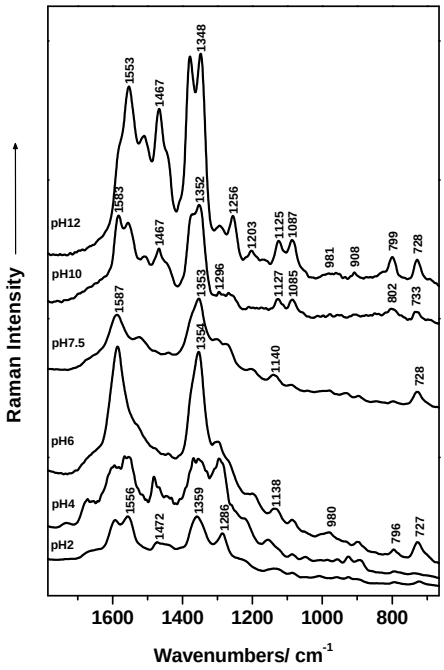

Figure 3.4: SERS spectra of the 10^{-4} M dacarbazine aqueous solution at different pH values. Excitation 532 nm.

Chapter 4

Raman and SERS investigations of healthy and diseased mouse skin

4.1 Introduction

Cancer in its earlier stages exhibits cells with an increased nucleus-to-cytoplasm ratio, deficiencies in their DNA structure, higher metabolic activity, and changes in lipid and protein levels [41], which differ from their healthy analogous. Raman microspectroscopy is suitable for cancer diagnosing because of its sensitivity in detecting these subtle biochemical changes. A first aim of the present study was to investigate various mouse skin pathologies using Raman microspectroscopy.

Chemoprevention implies the administration of agents with the aim of preventing the mutational and promotional events that occur during the abnormal proliferation of cells [42]. At the moment, there is a constant search for new drugs that can be used as chemopreventive agents in the treatment of cancer [43]. In the present study, the chemopreventive activity of natural compounds extracted from the outer bark of the Betula birch tree has been investigated. Raman spectroscopy has been further used for monitoring the molecular changes induced by the treatment based on the natural products anti-cancer candidates at the skin level. Accurate monitoring of the clinical treatment is essential for the quality of life, performance index and survival of patients. The clinical field is in great need for optical imaging techniques that can be used non-invasively and in a rapid manner [44]. Thus, it is crucial to develop sensitive techniques that can diagnose the diseases and directly monitor treatment induced modifications. The great appeal of Raman microspectroscopy recently applied in the biomedical field lies especially in its potential for *in vivo* applications.

The first part of this study presents *in vivo* applications of Raman microspectroscopy for the detection and characterisation of various mouse skin pathologies. The rodents investigated here were classified into four groups: the melanoma group (resulted following the the treatment with the chemical carcinogen 7,12-dimethylbenzanthracene (DMBA) as initiator and 12-O-tetradecanoylphorbol-13-acetate (TPA) as cancer promoter), the control group, which was kept healthy, the betulin nanoemulsion group, which was treated with the betulin nanoemulsion previously characterised (see Sections 2.2.2 and 2.2.3) after the application of the cancer initiator DMBA, and the acetone group, which was employed as control for possible solvent induced biochemical modifications. The experiment is part of a large multidisciplinary approach, where reproducible melanoma has been obtained in mice and new betulin-based pharmaceutical formulations with potential efficacy in treating skin cancer have been prepared and tested. Raman microspectroscopy was employed as a non-invasive, label-free optical method for the *in vivo* monitoring of the effects of the betulin nanoemulsion penetration and for the investigation of the molecular changes that occur at the skin level of the rodents, subsequent to the chemical treatment.

It is well known, however, that the Raman scattering is a weak effect [45]. Moreover, the Raman signal of biological samples is overlapped by the auto-fluorescence of the samples [46]. Surface enhanced Raman

spectroscopy (SERS) can be employed to amplify the weak Raman process by using metallic nanoparticles. The enhanced Raman signal is due to combined electromagnetic and chemical mechanisms involving the adsorbate and the metal surface [47]. The capability of the SERS technique has been demonstrated recently for biomedical applications [48–50], thus the following aim of this study was to use the SERS technique for the amplification of the Raman signal acquired from mouse skin tissues. Here, SERS effect is employed for both *in vivo* and *ex vivo* applications in biological skin tissues. A SERS characterization of the mouse skin samples is provided, as well as an attempt to elucidate the SERS mechanism resulted from the biological samples.

Nanobiosensors are relatively a new class of biosensing devices which have the capacity for sensitive local chemical probing of native biological molecules in living systems [51]. The development of nanosize labels used for cell biology and bio-chemistry applications is currently a major research focus [52,53]. The most basic SERS labels are composed of a Raman reporter molecule attached to Au or Ag nanoparticles [54]. These labels can be inoculated into cells or tissues and based on the SERS signature of the attached molecule, the nanosensors can be localised [49, 55, 56]. Additionally, SERS contribution is obtained from the immediate vicinity of the the label [57]. The inoculation of reporter molecules together with Au/Ag nanoparticles inside organisms or cells might enable the identification of sensitive chemical modifications in their immediate nano-environments. The aim of this study was to acquire the signal from SERS labels based on Ag nanostructures decorated with cresyl violet Raman reporter molecules buried into biological tissues. Cresyl violet (CV) dye was used as the Raman reporter molecule due to the high enhancement observed from its vibrational modes adsorbed to metallic nanoparticles.

4.2 Results and discussions

4.2.1 *In vivo* Raman characterisation of mouse skin specimens

Averaged Raman spectra were calculated for each of the four groups with the aim of identifying the main differences observed between the spectra and the Raman marker bands characteristic to each treatment, as well as the similarities between the groups (Fig. 4.1).

Control and the solvent treated rodents

The most intense bands observed in the control skin averaged Raman spectrum (Fig. 4.1 label N) are the amide I at 1657 cm^{-1}, the CH_2CH_3 bending in proteins and lipids at 1445 cm^{-1}, the amide III of collagen at 1270 cm^{-1}, the C-C backbone stretch of lipids or C-N stretch and C-O stretch of proteins and carbohydrates at 1128 cm^{-1}, the phenylalanine band at 1003 cm^{-1}, the C-C stretch in proteins around 936 cm^{-1}, and the amino acids band at 855 cm^{-1} [58–60]. In the high wavenumber region, lipids bands are observed at 2850 and 2880 cm^{-1}, and CH_2 asymmetric stretching vibrations at 2934 cm^{-1}. Collagen modes are present throughout the entire spectral region, suggesting that collagen is the main component in the investigated skin [61].

The characteristic spectrum of the acetone treated group (Fig. 4.1 label A) shows similar vibrational modes to the normal Raman spectrum, however a small decreases in the relative intensity of the amide I and III bands can be observed. Additionally, these modes present a shift towards lower wavenumbers, 1655 and 1265 cm^{-1}, while the CH_2 CH_3 bending mode of proteins and lipids shows a slight shift towards higher wavenumbers (1448 cm^{-1}).

Carcinogens (TPA-DMBA) and betulin nanoemulsion treated rodents

The averaged Raman spectra of the skin treated with the carcinogens on one hand, and the betulin nanoemulsion after the carcinogen initiator on the other hand, are presented in Fig. 4.1 labels TD and BE, respectively. A molecular composition change in proteins is suggested by the decrease of the amide I band observed in these spectra, as well as the shift of the CH_2CH_3 bending mode of proteins and lipids

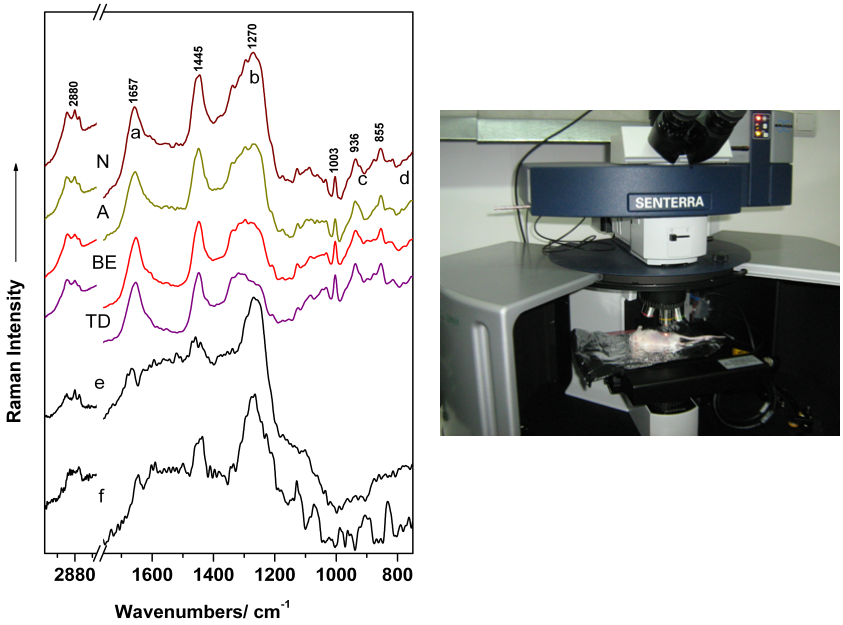

Figure 4.1: (left) Average Raman spectra of the normal (N), melanoma (TD), acetone (A) and betulin (BE) treated groups. Spectral alterations of the following Raman bands and spectral intervals are indicated: (a) the amide I band of proteins, (b) the amide III band region around 1270 cm^{-1} showing a decrease from the N spectrum and the nucleic acids-lipid 13001340 cm^{-1} region showing an increase in TD spectrum, (c) the C-C stretch in proteins around 936 cm^{-1} and (d) the 788 cm^{-1} band of DNA. (e) Representative difference spectrum between N and BE spectra and (f) difference spectrum between BE and TD. Spectrum (f) was multiplied by a factor of 2 for better visibility. (right) Photograph showing the laser beam focused at the skin level of an anesthetised rodent

towards higher wavenumbers. The main differences between the N and TD and BE spectra are observed in the 1240-1340 cm^{-1} spectral region. The TD spectrum shows a drastic decrease of the 1270 and 1244 cm^{-1} bands of amide III and an increase of the 1299 cm^{-1} (CH twisting and wagging vibrations in lipids), 1319 (attributed to both collagen and nucleic acids, more specifically to purine bases guanine and adenine [62]), and 1339 cm^{-1} (assigned to CH twisting and wagging in lipids or nucleic acids [58]) bands. The BE spectrum on the other hand, while presenting an increase of the 1270 cm^{-1} and the adjacent bands characteristic to amide III, a decrease of the lipids and nucleic acids bands to a similar relative intensity to the amide III bands is observed. The intensity increase of these modes in the TD skin suggests a change of molecular structures of proteins and a higher percentage of nucleic acids content in association to tumor transformations [63]. To better identify the molecular changes between the specimens, difference spectra were calculated. It was thus shown that the BE characteristic spectra present a higher relative intensities of the amide I and III of collagen bands, indicating a higher protein content.

The regions showing the main dissimilarities between the averaged spectra were further considered for investigation. Intensity ratios were calculated for these bands and the results were compared for different skin treatments. The following intensity ratios were selected for discriminating between the spectra:

$$r_1 = \frac{I_{1270}}{I_{1330}}; r_2 = \frac{I_{1660}}{I_{1445}}; r_3 = \frac{I_{788}}{I_{1003}} \tag{4.1}$$

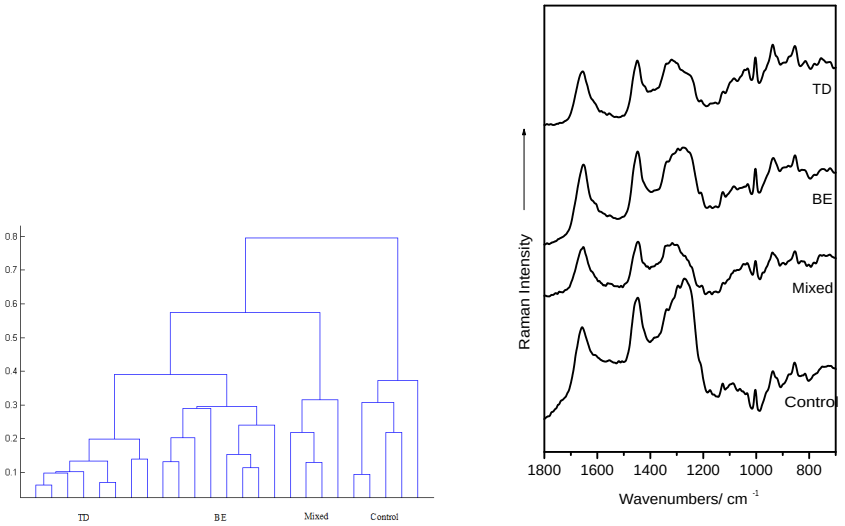

(a) (b)

Figure 4.2: (a) Dendrogram showing the separation of the Raman spectra with the resulted four clusters and (b) the clusters characteristic averaged Raman spectra

Hierarchical cluster analysis (HCA) was applied to the pre-processed spectra and this grouped them in four clusters: the TD cluster (grouped 75% of the melanoma spectra), the BE cluster (77% of the betulin nanoemulsion treated skin spectra and one sixth of the melanoma spectra), the mixed cluster (composed of the remaining melanoma and betulin nanoemulsion spectra and 30% of the acetone treated skin spectra) and the control cluster (composed of the healthy skin spectra and the remaining 70% of the acetone spectra). K-means was further employed for verifying the HCA clustering result and the obtained averaged Raman spectra characteristic to each cluster are presented in Fig. 4.2b.

The melanoma (TD) skin group was characterised by increased concentrations of nucleic acids, high intensity of the amide I band relative to the CH_2 band of proteins and lipids, and very low content of carbohydrates. Similar trend was previously identified in other studies for cancerous regions [60,62]. Thus,

it can be concluded the TD cluster corresponds to cancerous skin and that the chemical treatment (TPA and DMBA) induced a decrease of the collagen content, accompanied by an increase of the nucleic acids and lipids content. The Raman spectra acquired from the healthy rodents group and most of the acetone treated one were grouped in a second cluster. Some of the spectral features characteristic to this group indicated high content of amide III of collagen and of carbohydrates, and decreased content of the amide I band in comparison to the previous clusters. Most of the Raman spectra collected from the betulin treated rodents were grouped with a small percentage of the TD spectra in a third cluster. This group exhibited high content of amide III of collagen and higher content of carbohydrates, suggesting that the betulin nanoemulsion had a beneficial effect on the carcinogens treated skin. Additionally, it suggested the possibility that the induced melanoma did not spread out homogeneously over the entire skin surface and some regions could still be in a very early phase of development, pathologically similar to the betulin treated skin. The fourth group composed of Raman spectra characteristic to the betulin nanoemulsion treated skin, the melanoma skin and the acetone treated skin, enforces the supposition that the applied treatments showed different effect in different regions of the skin.

Concluding, the ability of the *in vivo* Raman spectroscopy for therapy monitoring is demonstrated and the Raman results indicate a beneficial bioactivity of the betulin nanoemulsion, confirmed by the histopathological investigation. The betulin containing nanodroplets penetrated the skin, leading to molecular modifications which, pathologically speaking, indicated the reduction of the inflamed areas and inhibition of the malignancy. The main conclusion of present study is that betulin could be applied as a prophylactic and therapeutic compound in skin pathology, especially in skin lesions.

4.2.2 Tissue screening using surface enhanced Raman spectroscopy

With the development of nanotechnology, different types of metallic nanoparticles have been synthesised and their benefits for biomedical applications have been extensively studied [53, 54, 64, 65]. The implementation of nanosensors in early detection of disease and subsequent targeting of treatments may result in more successful patient outcomes and reduce treatment side effects. Considering the very sensitive Raman detection and the capacity of SERS to acquire spectral information from the immediate vicinity of nanostructured materials, gold and silver nanoprobes based on SERS can be ideal tools for the investigation of small morphological structures in cells, tissues and even living organisms.

In vivo and *ex vivo* SERS tracking

To determine whether SERS spectra can be acquired from nanoparticles buried in animal tissues, small dosages of silver nanoparticles were injected subcutaneously in live rodents and the signal was acquired from the respective points. Fig. 4.3 presents the Raman and the SERS signal acquired from a spot where nanoparticles were injected. Employing the confocal function of the instrument, the laser was focused on the surface of the skin and 3 measurements were selected at the same x-y position but at different sample depths (on the z axis). The distance between the individual measurements was 1000 μm. Using the 50 x 1000 μm confocal aperture with the 50 x objective, a depth (axial) resolution of 3.2 mm could be obtained.

The first two spectra exhibit the characteristic Raman signal of tissues and are very similar to each other, which indicates that due to the high axial resolution, the signals were acquired from basically the same point. However, when the stage was moved at 3000 μm depth from the surface, it was possible to acquire signal from the skin layers closer to the injected nanoparticles. Spectrum (c) presents new peaks, as well as a higher intensity compared to the previous two Raman spectra. One of the main difference between the spectra is the decrease in intensity of the amide I band of proteins at 1646 cm^{-1} in the spectrum acquired from the biomolecules in the vicinity of the silver nanostructures. New amplified bands are measured at 1554 cm^{-1} with a shoulder at 1575 cm^{-1}, the weaker 1495 cm^{-1} band, the intense, sharp 1343 cm^{-1} with shoulders at 1304, 1269, and 1222 cm^{-1}, the 1134, 1056, 719, and 656 cm^{-1}, as well as the high intensity 220 cm^{-1} band. According to the SERS selection rules [66], the vibrational modes

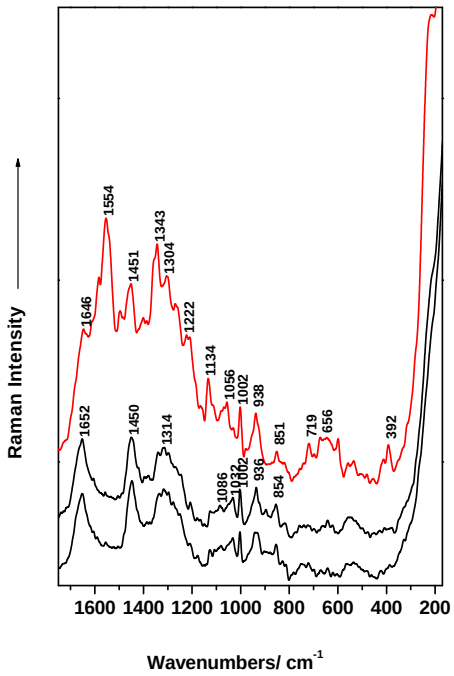

Figure 4.3: Raman (bottom black spectra) and SERS spectra (upper red spectrum) acquired from different depths inside the skin layers from a spot where the silver nanoparticles were injected.

with the polarizability component perpendicular to the metallic surface are enhanced in the SERS spectra. A tentative assignment of the main bands observed in the SERS spectrum is proposed based on the current literature [58,67–70]. Bands assigned to nucleic acids are located at 719 cm^{-1} (adenine), 1056 cm^{-1} (DNA backbone), 1222 cm^{-1} (guanine), 1269 cm^{-1} (cytosine), 1343 cm^{-1} (adenine), 1575 cm^{-1} (thymine and guanine). Proteins are observed at 1554 cm^{-1} (amide II), 1451 cm^{-1} (CH_2CH_3 deformation), 1343 cm^{-1} (CH_3CH_2 wagging of collagen), 1134 cm^{-1} (proline), 1002 cm^{-1} (phenylalanine), 938 cm^{-1} (C-C ring stretching vibrations of proline), 656 cm^{-1} (C-C stretch of proteins), while lipids are seen at 1451 cm^{-1}. Another new band is the 227 cm^{-1} representative to the Ag-N mode when N-containing molecules are adsorbed to the Ag nanosurface [67]. The high-quality SERS spectra obtained in this case demonstrate the capability of the SERS technique for *in vivo* biomedical applications, which open up a whole new research direction [64]. However, further experiments need to be conducted for stabilising the acquired SERS signal and characterising various skin pathologies, as well as toxicology studies related to the bioactivity of the silver nanoparticles. In our case, the mice specimens were sacrificed following the experiments.

The further aim of this research was to probe the Raman enhancement using Ag colloidal nanoparticles uptake by the formalin fixed skin tissues, collected following the autopsy of the previously investigated rodents by *in vivo* Raman spectroscopy. Previously, our group has demonstrated the SERS effect acquired from formalin fixed skin tissues by recording SERS maps of the skin samples [13]. At that time, it was demonstrated that the SERS spectra were acquired only from scattered points in the Raman image, and that the signal differed from one point of acquisition to another, meaning that the nanoparticles were scattered throughout the tissue. To begin with, healthy skin tissue fixed solely in formalin solution were investigated in order to check for any modifications that the fixation procedure might induce. Following the investigations, it was concluded that the formalin fixation induced no visible major modifications which might hinder the analysis of the skin tissues.

Further studies were performed with the aim of amplifying the Raman signal of the skin tissue by

employing silver nanoparticles. High-quality, reproducible SERS signal was obtained *ex vivo* from mouse skin and the tissue pathology could be differentiated. The variability of the spectra was calculated from the correlation coefficients obtained according to the spectral correlation function presented by Barhoumi *et al.* [71]. The results suggested that the SERS spectra recorded from the melanoma skin samples were the most reproducible ones. Thus, for a better differentiation of the SERS signal corresponding to each of the treatments, the SERS spectra were further averaged (Fig. 4.4). The main bands observed in all spectra are measured at 1572, 1440, 1329, 1220, 1128, 956, 821, 721, 654, 483, and 232 cm^{-1}.

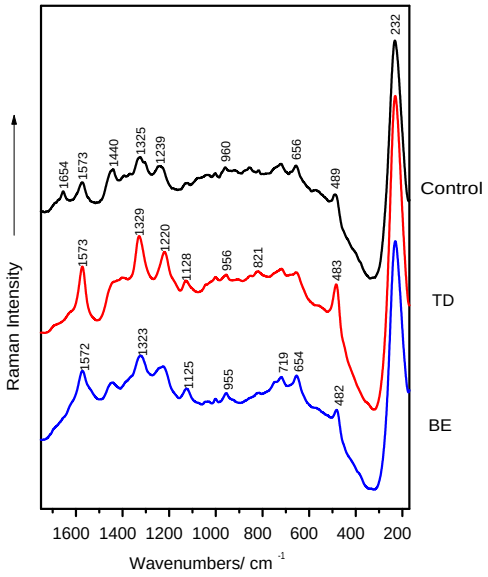

Figure 4.4: Comparison between the averaged SERS spectra acquired from the control, carcinogens treated (TD), and betulin nanoemulsion treated (BE) skin samples.

The intensity differences observed between the vibrational modes in the SERS spectra characteristic to the various skin pathologies allowed the characterisation of normal, melanoma, and betulin nanoemulsion treated skin samples. The main SERS biomarkers chosen for the differentiation of the spectra were the 722 and 655 cm^{-1} bands of nucleic acids, whose ratio indicated an increase in the melanoma characteristic spectra compared to the healthy ones, in agreement with previous studies [70, 72] and the *in vivo* Raman investigation, although other subtle differences were also observed. The same results were obtained for the second SERS study which involved autopsy skin tissues collected from four mice groups: a healthy, a melanoma, and two groups treated with medications based on inclusion complexes of the main birch bark natural compounds with cyclodextrins (betulin and betulinic acid).

Tracking and detecting optical nanosensors in mouse skin tissues

The last part of this study focused on on the development of optical nanosensors based on Ag nanoparticles. SERS labels based on Ag nanostructures decorated with cresyl violet Raman reporter molecules were developed and buried into biological tissues with the aim of tracking them inside the skin tissues. The results showed amplified Raman signal of tissue specific components in addition to the SERS signal of the cresyl violet label.

Fig. 4.5 presents a series of SERS spectra recorded from the skin tissue injected with labeled and unlabeled Ag nanoparticles, respectively. The SERS spectral signature of the CV Raman label is also presented for eye guidance (spectrum 9). The recorded signal from the skin samples is the sum of the

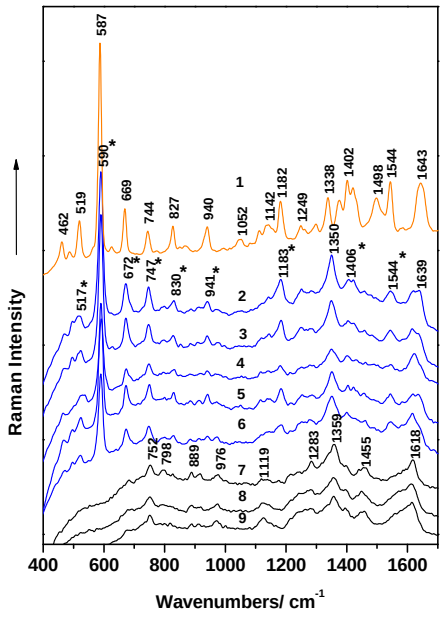

Figure 4.5: Representative SERS spectra collected from skin tissue injected with CV labeled Ag nanoparticles (1-5) and unlabeled Ag nanoparticles (6-8). The SERS spectrum of the CV Raman label is given for eye guide (9). Asterisks denote CV characteristic bands. Excitation 632.8 nm, 1 s integration time, 4 acquisitions.

auto-fluorescence background and the fingerprint signal of the tissue resulted from the excitation with the visible laser line (633 nm). The reproducible main bands observed in the SERS spectra of the tissues (spectra 6-8) are located at 1618, 1455, 1359, 1283, 1119, 976, 889, 798 and 752 cm^{-1}. These peaks are assigned to proteins (889 cm^{-1}, 1119 cm^{-1} C-C stretching mode of lipids and proteins, 1283 cm^{-1} amide III, 1455 cm^{-1} CH deformation) and nucleic acids (798 cm^{-1} O-P-O stretching mode of DNA, 1359 cm^{-1} guanine).

The inoculation of the optical nanosensors in skin tissues allowed for SERS tracking based on the spectral signature of the Raman reporter molecule. The fingerprint band at 590 cm^{-1} characteristic to CV can be clearly detected in the SERS spectra, among other vibrational modes characteristic to the dye molecule. However, since the SERS labels were not protected by any surrounding layers, the molecules in the medium were free to adsorb on them [54]. Although their molecular signature decreased compared to the SERS spectra acquired from the unlabeled Ag nanoparticles, the SERS spectral signature of the skin tissue can still be detected along with that of the Raman reporter. This is further demonstrated by the broadening and shifting observed for several bands characteristic to the double amino functionalised CV nanotags. These vibrational modes were assigned to NH vibrations, indicating that the previously free amino groups interacted with tissue components.

4.3 Conclusions

This study shows that Raman spectroscopy can be successfully applied for the *in vivo* characterization and differentiation of skin pathologies, as well as for monitoring the locally applied skin treatment. The clustering methods, hierarchical clustering analysis and k-means clustering, distinguished and identified the main biochemical differences between the rodents and grouped the spectra into four clusters. The melanoma (TD) skin group was characterised by increased concentrations of nucleic acids, high intensity

of the amide I band relative to the CH_2 band of proteins and lipids, and very low content of carbohydrates. The Raman spectra acquired from the healthy rodents group and most of the acetone treated one were grouped in a second cluster. Some of the spectral features characteristic to this group indicated high content of amide III of collagen and of carbohydrates, and decreased content of the amide I band in comparison to the previous clusters. Most of the Raman spectra collected from the betulin treated rodents were grouped with a small percentage of the TD spectra in a third cluster. This group exhibited high content of amide III of collagen and higher content of carbohydrates, suggesting that the betulin nanoemulsion had a beneficial effect on the carcinogens treated skin. Additionally, it suggested the possibility that the induced melanoma did not spread out homogeneously over the entire skin surface and some regions could still be in a very early phase of development, pathologically similar to the betulin treated skin. The fourth group composed of Raman spectra characteristic to the betulin nanoemulsion treated skin, the melanoma skin and the acetone treated skin, enforces the supposition that the applied treatments showed different effect in different regions of the skin.

Further studies were performed with the aim of amplifying the Raman signal of the skin tissue by employing silver nanoparticles. High-quality, reproducible SERS signal was obtained both *in vivo* and *ex vivo* from mouse skin and the tissue pathology could be differentiated. The *in vivo* results suggest the amazing capability of the technique for biomedical applications, however further toxicology studies need to be performed. The SERS spectra presented amplified bands characteristic mainly to nucleic acids modes and proteins, and it was concluded that a possible interaction between N-atoms containing molecular components and the Ag nanoparticles had taken place. The SERS spectra allowed the differentiation of the various skin pathologies and the characterization of the normal, melanoma, and betulin nanoemulsion treated skin samples. The main SERS biomarkers chosen for the differentiation of the spectra were the 722 and 655 cm^{-1} bands of nucleic acids, whose ratio indicated an increase in the melanoma characteristic spectra compared to the healthy ones, in agreement with previous studies and the *in vivo* Raman investigation, although other subtle differences were also observed.

The last part of this chapter presented the preliminary results on the development of optical nanosensors based on Ag nanoparticles. The characterization of the SERS labels based on CV Raman reporter molecules and Ag nanoparticles is presented, and it is shown that the nanosensors can be tracked inside skin tissues. The nanosensors can be localised based on the SERS fingerprint band of CV at 590 cm^{-1}. Moreover, SERS tissue bands were detected as well, indicating that tissue specific molecular compounds adsorbed on the unprotected labels. This is further demonstrated by the broadening and shifting observed for several bands characteristic to the double amino functionalised CV nanotags. These vibrational modes were assigned to NH vibrations, indicating that the previously free amino groups interacted with tissue components resulting in double amino functionlised nanoparticles.

Chapter 5

Raman microspectroscopy of stem cells

5.1 Introduction

Stem cell research has gained much appreciation in recent years due to the beneficial potential of stem cells to transform the modern clinical medicine when dealing with difficult diseases which are currently incurable. During embryonic development, cells are continually gaining new phenotypes and loosing old ones. This ability of a cell to change its activities depends on the synthesis of new species of RNA and implicitly on the synthesis of new species of proteins. An undifferentiated cell is one that does not have a certain specialization. Human embryonic stem cells (hESCs) are cells that originate from the inner cell mass of the embryo and they have two main properties, the ability for self-replication and for generating daughter cells that turn into differentiated cells.

The identification of specific markers is essential in following the differentiation process of ES cells and for the characterisation of their progenies. The current approaches to characterise stem cells and their differentiation progenies are invasive, employ time-consuming techniques and require fixation of the cells. Therefore, at the moment there is a great need for new methodologies which can be employed to characterise and monitor the differentiation process and quantify key biomarkers in a non-invasive, rapid manner.

The use of micro-Raman spectroscopy for the characterisation of stem cells [73] and the discrimination between undifferentiated and differentiated cells [74] relies on the biochemical and biophysical cellular modifications that take place during the differentiation process. The attractiveness of RMS is that it can be used to measure biochemical differences without the use of labels or other invasive procedures. Moreover, the combination of Raman microspectroscopy, which reflects the local biochemical composition for a given optical focus with immunofluorescence, which can offer high-spatial resolution information about previously specified cell components, ensures a precise characterization [73, 75, 76]. The large number of Raman spectral data can be used to construct images based on the biochemical abundance of the samples [77]. Data processing methods such as PCA or LDA and clustering methods such as K-means analysis or hierarchical cluster analysis (HCA) can be employed to analyse this information [78–80]. According to the specific phenotype that a cell differentiates into, it produces the required proteins which allow the cell to function accordingly. During the differentiation process of murine ES cells into embryoid bodies (EBs), the most significant observed differences were related to nucleic acids [81,82]. A decrease of 25% in the magnitude of the RNA peak at 813 cm^{-1} was observed in the differentiated EBs in comparison to the undifferentiated ES cells. Spectral differences related to nucleic acids and proteins were observed in the differentiation process of human ES cells, as well [79]. The Raman markers of tryptophan at 757 cm^{-1} and DNA/RNA O-P-O stretching vibrations at 784 cm^{-1} were effective in discriminating between the phenotype of the investigated cells. Cytoplasmic RNA in undifferentiated neural stem cells was related to the biochemical differences observed between undifferentiated neural stem cells (NSCs) and NSCs derived glial cells [83]. The Raman spectral images revealed cytoplasmic regions with concentrations of RNA as high as 4 mg/ml in NSCs, and $\sim$ 1 mg/ml in glial cells.

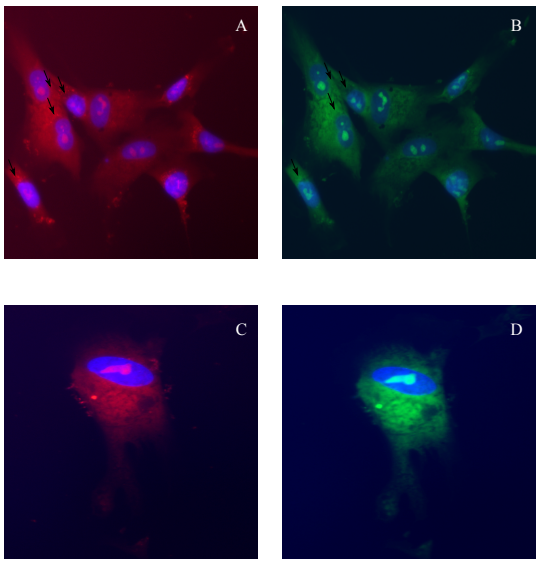

Figure 5.1: Immunofluorescence images of fibroblasts cells showing the ribosomal protein S3 in red (A and C, ribosomal protein S3 antibody), RNA in green (B and D, SYTO RNA select), and the nuclei in blue (DAPI).

The recent discoveries of the biochemical Raman spectral markers during the differentiation process of stem cells has been the main motivation for carrying out this study. Here we applied the capability of Raman microspectroscopy and immunofluorescence techniques to detect these biomarkers in human embryonic stem cells and their fibroblasts derivatives. High spatial resolution Raman images were used to map the distribution of the nucleic acids key biomarkers.

5.2 Results and discussions

5.2.1 Raman microspectroscopy and immunofluorescence of cells

A first aim of this study was to establish the exact origin of the increased cytoplasmic RNA content detected in undifferentiated cells during the Raman microspectroscopy monitoring of the differentiation process in stem cells [83]. The origin of the RNA was probed in cells by acquiring fluorescence images. The comparison (Fig. 5.1) between the IF images showing the ribosomal protein S3 (left, red) and the total amount of RNA (right, green) suggests that most of the detected RNA is in fact ribosomal RNA.

5.2.2 The identification of nucleic acids Raman biomarkers in hESCs and fibroblasts cells

The main aim of this study was to detect RNA characteristic Raman signals in the analysed cells and monitor its intracellular distribution. Principal components analysis (PCA) proved helpful in minimising the dimension of the Raman data set while keeping most of the variation. Thus, in some of the investigated hESCs, PCA identified RNA characteristic Raman signal and its distribution in the cells could be monitored by reproducing the corresponding Raman images. The RNA PC identified in the Raman data acquired from a typical fixed hESC and its distribution plotted at each position in the cell is presented in Fig. 5.2B and E.

The comparison between the Raman spectral images corresponding to specific biomolecules and the fluorescence staining pattern, allows a better correlation between the molecular information found in the Raman spectra and the cellular components. Compared to the DAPI staining (image H in Fig. 5.2), the cell region showing high 788 cm^{-1} band area in the coresponding Raman image (image C in Fig. 5.2) is

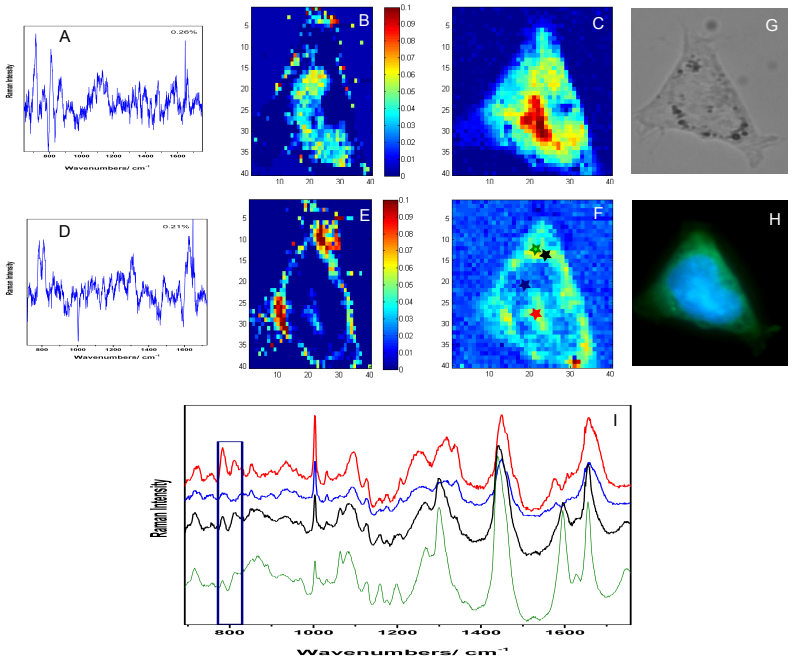

Figure 5.2: The PCs showing DNA (A) and RNA Raman signal (D) and the Raman images reproduced by plotting them at each position in the cell (B and E, respectively). The Raman images corresponding to the 788 cm^{-1} (C) and 813 cm^{-1} (F) band area for a typical fixed hES cell and the optical (G) and fluorescence image (H) of the cell showing the nucleus in blue (stained with DAPI) and RNA nucleic acids in green (stained with SYTO RNA select). Individual Raman spectra (I) collected from the star marked positions in the nucleus and the cytoplasm.

larger than the cell nucleus, which was expected since this band is assigned to cytosine and uracil ring vibrations, as well as O-P-O symmetric stretching vibrations of DNA [84]. It can be thus concluded, that the Raman image showing the distribution of the 788 cm^{-1} band area presents regions rich in both DNA and RNA. The high intensity region seen in the corresponding Raman image of the PC carrying the DNA characteristic Raman signal (Fig. 5.2 B) on the other hand, correlates much better with the DAPI staining of the cell nucleus. This is due to the fact the the Raman image was reconstructed by plotting the entire DNA representative spectrum, thus reproducing a more accurate image of the nucleus. Plotting solely the band area of the 788 cm^{-1} can not be accounted for the true distribution of the RNA inside the cells, however, since this band is also assigned to the O-P-O stretching vibrations of DNA. This can be seen especially in the high intensity 788 cm^{-1} band area assigned to the cell's nucleolus, where the Raman image shows very intense regions, due to the overlapping signal of both RNA and DNA, as well as in the regions corresponding to the rest of the nucleus which have a medium intensity in the Raman image, but do not match the RNA pattern shown by the fluorescence image.

The comparison between the Raman images showing the RNA distribution reproduced either by plotting the 813 cm^{-1} band area (image F), or the PC carrying the RNA representative Raman signal (image E in Fig. 5.2), correlate well with the SYTO RNA staining pattern. High intensity RNA regions are seen especially in the nucleolus and scattered through the cytoplasm, while the nucleus shows decreased RNA content, as it can be seen in the Raman spectra presented in Fig. 5.2I. Looking at the individual Raman spectra, it can be easily noticed that the 813 cm^{-1} band appears in the nucleolus and is absent in the nucleus. This is in accordance with the fluorescence image showing the intracellular distribution of the RNA.

However, not all the investigated hES cells exhibited such high nucleic acids concentrations. Most of them showed poorly resolved 813 cm^{-1} RNA peaks, seen as weak bands, or overlapped by the Raman

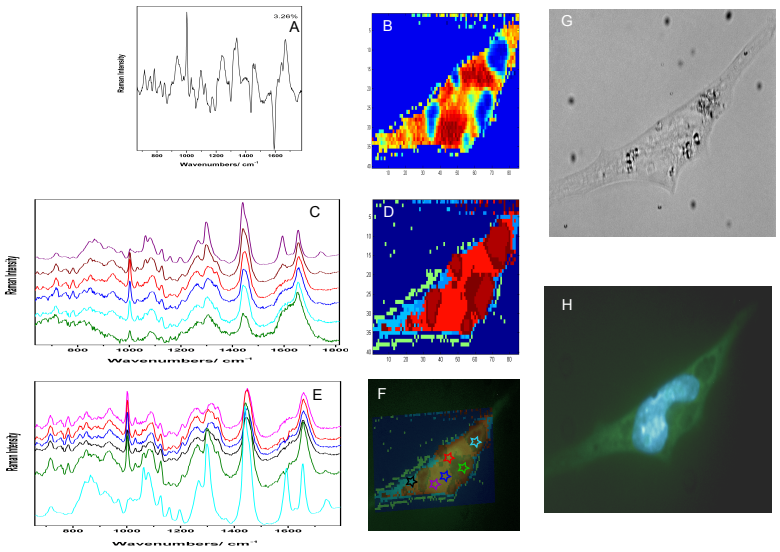

Figure 5.3: The PC showing nucleic acids characteristic Raman signals (A) and the Raman image reproduced by plotting the PC (B), the K-means clustering Raman image (D) and the color coded K-means clusters averaged Raman spectra (C) and the overlaid K-means and fluorescence image showing the RNA distribution pattern (F) and individual Raman spectra collected from the star marked positions (E). Brightfield image of the cell (G) and the fluorescence image (H) showing the nucleus in blue (DAPI) and RNA in green (SYTO RNA Select).

signal of other biomolecules. PCA analysis could still detect nucleic acids signals, although most of the times mixed with signals from other biomolecules, usually proteins. Fig. 5.3 presents the PC showing nucleic acids characteristic Raman signal along with the reproduced Raman image. Comparing the DAPI staining with the Raman image showing the distribution of the PC, it can be easily observed that the high intensity regions in the Raman image correspond to the cell nucleus.

K-means clustering was applied to group similar Raman spectra into clusters (Fig. 5.3D). Despite the well separation of components shown by K-means clustering, the only nucleic acids bands measured in the spectra were located at 788, 1090, and 1340 cm^{-1}. To ease the correlation between the Raman image and the fluorescence one, the K-means Raman image was overlapped with the SYTO RNA select fluorescence image (Fig. 5.3F) and Raman spectra collected regions inside the cell showing high intensity RNA in the fluorescence image were further analysed in detail. The 813 cm^{-1} band presents a slight intensity increase in the spectra collected from the cell's nucleoli (spectra red and magenta). Additionally, a shoulder was measured at 1577 cm^{-1}, too. Following the same trend as in the previously investigated cells, the 813 cm^{-1} band decreases drastically in the Raman spectra collected from the nucleus (blue spectrum). The Raman spectra acquired from the cytoplasmic areas showing high RNA content in the fluorescence image (green areas) exhibited similar spectral pattern in the 780–850 cm^{-1} region to the spectra acquired from the nucleoli and a weak shoulder was observed at 813 cm^{-1}. On the contrary, the dark regions in the fluorescence image matched the high lipids and lysosomes regions in the Raman image and the characteristic Raman spectra showed much lower to no nucleic acids signal (cyan and green spectra).

Previous Raman studies investigating the differentiation process of stem cells into specific phenotypes concluded that the most significant differences between undifferentiated and differentiated cells were related to nucleic acids [81–83, 85]. The differentiation process implies changes of biochemicals which induce new properties to the differentiated cells. With this aim, the RNA is used for converting the genetic information into amino acid sequences. Thus, modifications of the characteristic Raman spectra are expected. Raman spectroscopy and fluorescence imaging were further applied to investigate the hESCs derived fibroblasts cells. The Raman image reproduced by plotting the 788 cm^{-1} band area extends as in

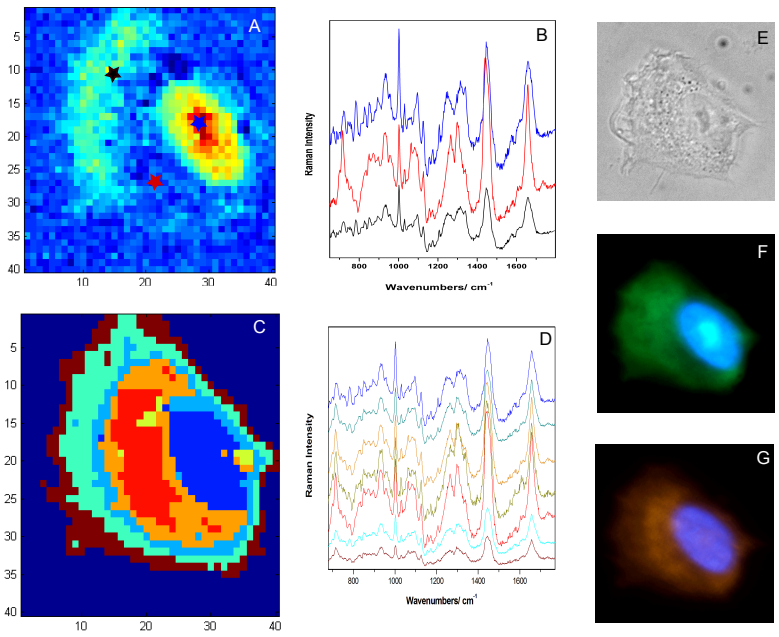

Figure 5.4: Raman spectral images corresponding to the 788 cm^{-1} band (A) and K-means analysis (C) of a typical fixed fibroblast cell. Individual Raman spectra taken from the star marked positions (B) inside the nuclei (blue stars) and cytoplasm (red stars) and color coded K-means clusters characteristic Raman spectra (D). Bright field and fluorescence images (E and F) showing DAPI in blue, SYTO RNA in green, and ribosomal protein S3 antibody in red.

the previous cases over the DAPI staining region. The blue spectrum collected from the nucleus (image B) shows a well resolved 788 cm^{-1} band, while the Raman spectrum characteristic to the cytoplasm presents a content rich in lipids and poor in nucleic acids (red spectrum). A drastic decrease of the intensity of the 788, 1096, and 1576 cm^{-1} bands assigned to nucleic acids is observed in this spectrum. However, the Raman image shows medium intense regions located in the cytoplasm which also show nucleic acids characteristic Raman signals (black spectrum) and which are probably assigned to RNA rather than DNA, which is usually localised in the nucleus.

K-means analysis was applied to group regions inside the cells of similar biomolecules compositions and concentrations, with the aim of monitoring the intensity variation trend of the nucleic acids Raman bands. The highest intensity characteristic nucleic acids Raman bands are observed in the spectra corresponding to the nuclei of the cell (dark blue cluster in Fig. 5.4 C). Additionally, relatively high intensity nucleic acids Raman bands are observed in the peripheral membrane (cyan cluster). However, the 788 cm^{-1} band, as well as other Raman bands assigned to nucleic acids decrease quickly in intensity in the spectra collected from other regions. Despite the Raman results, the corresponding IF images still indicate the presence of RNA and RPS3. These observations suggest that the concentration of nucleic acids, and especially RNA, may have decreased in the differentiated fibroblasts cells until reaching a threshold below the detection limit of our instrument.

The RNA and nucleic acids content decrease observed in the fibroblasts differentiated cells was confirmed by calculating a difference spectrum between the averaged Raman spectrum of hESCs showing high RNA content and that of fibroblasts cells and the result is shown in Fig. 5.5 upper spectra. A comparison between the difference spectrum and the Raman spectra of DNA, RNA, and HSA proteins acquired from water solutions are also presented for comparison (Fig. 5.5 lower spectra). Raman bands associated to the DNA and RNA bases can be identified at 729 (adenine), 782, and 785 (uracil, cytosine), and 1578 cm^{-1} (guanine and adenine), while Raman bands assigned to the nucleic acid backbone observed

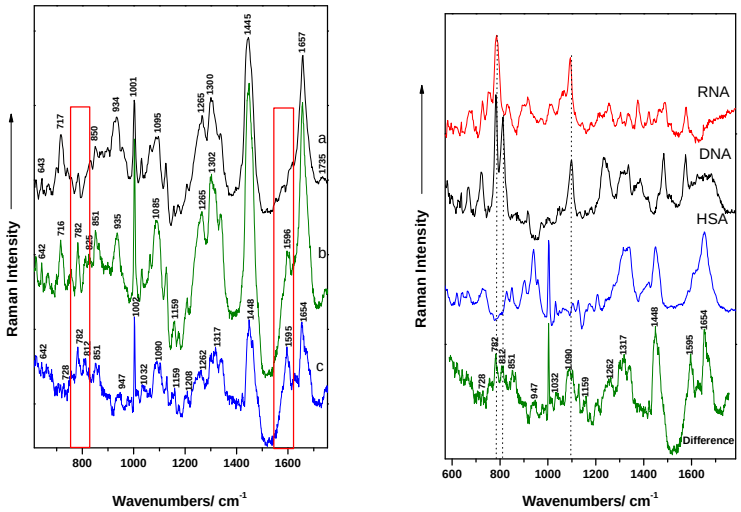

Figure 5.5: (left) Averaged Raman spectra characteristic to fibroblasts differentiated cells (a), hESCs showing high RNA content (b), and the computed difference spectrum (c). (right) Comparison between the Raman spectra acquired from water solutions of RNA, DNA, HSA protein, and the computed difference spectrum.

in both B-conformation DNA, as well as RNA are observed at 788 and 813 cm^{-1}. PO_2 vibrations are observed at 1090 cm^{-1}. Raman bands assigned to proteins were measured in the difference spectrum at 851 cm^{-1} (tyrosine), 947 cm^{-1} (proteins backbone), 1003 cm^{-1} (phenylalanine), 1654 cm^{-1} (amide I). In accordance with previous studies [81, 86], a higher content of nucleic acids, as well as proteins, was identified in the undifferentiated hESCs and this investigation indicates that the intracellular regions with the highest RNA content in the undifferentiated cells are the nucleoli and areas in the cytoplasm.

5.3 Conclusions

This study presents label-free Raman microspectroscopy investigations of human embryonic stem cells and their fibroblasts differentiated progenies. The investigations presented here identified nucleic acids biomarkers characteristic to the differentiation process in most of the analysed cells. For these, high RNA concentration areas were observed in the nucleoli and the cytoplasm of the undifferentiated cells, while a drastic decrease of nucleic acids, and in especially RNA, was observed in the Raman spectra acquired from the differentiated cells. The distribution of RNA and nucleic acids, was monitored by plotting at each position in the acquired Raman images, the band areas calculated for the 813 and 788 cm^{-1} bands, respectively. Additionally, it was shown the principal components analysis could also detect in these cells, RNA characteristic signals which correlated well with the fluorescence images showing the distribution of RNA or DNA, respectively.

The nucleic acids biomarkers could not be identified in all undifferentiated cells, however, either due to their lower concentration which decreased below the detection limit of our instrument, either due to the overlapping Raman signal from other biomolecules, such as proteins or lipids. In these cases, the band area of the 813 cm^{-1} could not be calculated and thus, the RNA distribution could not be monitored through the previous proposed methods. K-means analysis was employed to group regions inside the cells of similar biomolecules compositions and concentrations with the aim of observing the intensity variation trend of the nucleic acids Raman bands. A similar trend to the previous hESCs showing higher nucleic acids Raman signals in the nucleoli and the cytoplasm was identified.

Chapter 6

Conclusions

6.1 Conclusions

The main aim of this thesis was to show the capability of vibrational spectroscopies, and in especially of Raman spectroscopy, for pharmaceutical and biomedical applications. The main achieved targets are summarised here.

In the first phase, Raman spectroscopy was applied for the study of chemical entities with promising pharmaceutical properties for the treatment of skin diseases, natural extract compounds from the bark of the birch tree and dacarbazine, a drug already used for the treatment of skin cancer, especially melanoma. The second part of the thesis presents the in vivo and ex vivo Raman and SERS diagnoses and monitoring of mouse skin tissues of various pathologies resulted due to the chemical treatment and the natural compounds previously investigated. The monitoring of the treatment was based on the subtle bio-moelcular changes observed in the Raman and SERS spectra. The last part of the thesis addresses a new study based on the use of Raman microspectroscopy for the characterisation and identification of Raman biomarkers specific to the differentiation process in human stem cells.

The first study aimed at the vibrational characterisation of the natural compounds extracted from the birch bark and of their pharmaceutical formulations developed in order to improve their solubility. The main triterpenes in the birch bark and the natural extract were identified based on their spectral fingerprint and the fundamental triterpene was identified as betulin. The next target of the study was to provide a complete vibrational characterisation of betulin based on the experimental spectroscopic data and the density functional theory calculations (DFT). The betulinic acid and betulin inclusion compounds with cyclodextrins and nanoemulsions formulations obtained in order to improve the solubility of the triterpenes were further characterised spectroscopically. The formation of the 1:1 and 1:2 inclusion complexes was identified due to subtle spectroscopic changes observed in the FT-Raman spectra and it was concluded that betulin molecule interacts with the cyclodextrin cavity through the CH_2OH group.

The second study presented in this thesis is part of the same pharmaceutical applications area of vibrational spectroscopies and it was based on the pre-clinical development studies of dacarbazine, a currently used chemotherapeutic drug. The aim of this study was to gain more knowledge regarding the chemical and physical properties of this highly biomedical important molecule. A complete vibrational characterisation of the neutral, protonated, and deprotonated molecular species of dacarbazine employing IR, Raman, SERS, and DFT calculations was performed. The presence of the dacarbazine molecular species on the silver surface was observed in the SERS spectra and the NH_2 group was found to be involved in the chemisorption of the molecule, while a tilted orientation of dacarbazine to the silver nanosurface was identified.

The first biomedical application targeted here was the *in vivo* characterisation and differentiation of mouse skin pathologies, as well as the monitoring of the locally applied skin treatment using Raman spectroscopy. This target was achieved successfully and the work is summarised here.

A Raman spectral database was constructed based on the *in vivo* Raman spectra acquired from the

four mice groups employed in this study: a healthy one (N), one showing melanoma due to the applied chemical treatment (TD), one treated with acetone (A), and one treated with betulin nanoemulsion investigated previously (BE). The spectra analysis allowed the diagnosis of the skin pathologies, as well as monitoring the locally applied treatment at the molecular level. The main differences observed in the spectra characteristic to the melanoma skin compared to the spectra characteristic to the healthy skin represent the intensity increase of the Raman bands in the region 1240–1340 cm^{-1} attributed mainly to nucleic acids, the amide I band intensity increase relative to the CH_2 band of proteins and lipids, and a very low carbohydrates content. On the other hand, the characteristic spectra of the skin treated with the betulin nanoemulsion showed a high content of amide III of collagen band and high carbohydrates content, suggesting a beneficial effect of the betulin treatment.

A further aim of this study was to employ the SERS effect for the amplification of the weak Raman scattering of biological tissues. SERS signal was acquired *in vivo* by injecting Ag colloidal solution into the anesthetised rodents and recording the signal from the respective points. The confocal microspectroscopy allowed the acquisition of the Raman and SERS signal, respectively, at different depths inside the skin tissues. Moreover, SERS technique was employed for the *ex vivo* investigation of skin samples and various tissue pathologies could be differentiated and classified. The high-quality, reproducible SERS spectra were assigned based on the current literature and experimental SERS characterisation of nucleic acids. It was thus concluded that a possible interaction between N-atoms containing biomolecular components and the Ag nanoparticles had occurred.

The preliminary results involving the development of optical nanosensors based on metallic nanoparticles decorated with Raman reporter are presented. The SERS labels were probed for spectroscopic characterisation and tracking inside skin tissues. Tracking of the SERS labels inside mouse skin tissues was possible based on the spectroscopic fingerprint of the Raman reporter, here cresyl violet species, and in the process enhanced Raman signal characteristic to the biomolecular components attached to their surface or found in their very close proximity could be detected. Upon the cresyl violet species adsorption on the Ag nanoparticles, the molecular orientation with respect to the surface provided both amino functional groups free for tagging, resulting thus in double amino-functionalized Ag nanoparticles when inoculated into the biological tissue samples. This was indicated by the broadening and shifting observed for the Raman bands characteristic to the NH vibrations of the CV Raman label. These SERS markers could be successfully applied as SERS nanotags for the *ex vivo* studying of biomolecular skin components and reproducible SERS signal of nucleic acids and proteins was detected.

The second biomedical application presented in this thesis focused on label-free Raman microspectroscopy investigations of human embryonic stem cells and their fibroblasts differentiated progenies. The investigations presented here identified nucleic acids biomarkers characteristic to the differentiation process in most of the analysed cells. For these, high RNA concentration areas were observed in the nucleoli and the cytoplasm of the undifferentiated cells, while a drastic decrease of nucleic acids, and in especially RNA, was observed in the Raman spectra acquired from the differentiated cells. The distribution of RNA and nucleic acids, was monitored by plotting at each position in the acquired Raman images, the band areas calculated for the 813 and 788 cm^{-1} bands, respectively. Additionally, it was shown the principal components analysis could also detect in these cells, RNA characteristic signals which correlated well with the fluorescence images showing the distribution of RNA or DNA, respectively.

The nucleic acids biomarkers could not be identified in all undifferentiated cells, however, either due to their lower concentration which decreased below the detection limit of our instrument, either due to the overlapping Raman signal from other biomolecules, such as proteins or lipids. In these cases, the band area of the 813 cm^{-1} could not be calculated and thus, the RNA distribution could not be monitored through the previous proposed methods. K-means analysis was employed to group regions inside the cells of similar biomolecules compositions and concentrations with the aim of observing the intensity variation trend of the nucleic acids Raman bands. A similar trend to the previous hESCs showing higher nucleic acids Raman signals in the nucleoli and the cytoplasm was identified.

6.2 Future perspectives

Future developments are still required to increase the specificity of the Raman microspectroscopy technique for *in vivo* applications. A more complete Raman spectra data-base can be build, which could serve as a reference guide for future skin diagnosis. Even though these investigations have shown the beneficial activity of the natural compounds extracted from the birch bark for the treatment of skin lesions, future toxicity studies, as well as studies aimed at understanding the mechanism of action of these compounds at the molecular level are needed.

Due to the questionable effects of dacarbazine based treatment, as well as the numerous studies aimed at clarifying the physico-chemical properties of the molecular species of dacarbazine, future detection studies of various species of dacarbazine in different environments would be extremely important for the biomedical field. A preliminary study showing promising results was performed in this direction in the last period of this PhD, with the aim of detecting dacarbazine in cell cultures. It would be interesting to continue this study and investigate the biomolecular changes induced by dacarbazine at the cellular level in living cells.

The stem cells differentiation process characterisation study presents future perspectives for the label-free analysis of the differentiation process in stem cells using Raman microspectroscopy. The technique can be further improved by employing a Raman configuration system with higher spatial resolution. Moreover, further applications can be found for monitoring the development and growth of engineered tissue *in vitro*.

Further studies are required to establish the exact origin of the higher RNA concentration in undifferentiated cells and this could be achieved by overlapping higher spatial resolution Raman and fluorescence images showing the RNA distribution. Additionally, a spectral fitting model can be further improved, for achieving a precise fitting of the chosen biomolecular components characteristic Raman spectra to the spectra of the cells.

Bibliography

[1] S. Cutler and H. Cutler, editors, *Biologically active natural products: Pharmaceuticals* (CRC Press LLC, 2000).

[2] J. Drews, Science **287**, 1960 (2000).

[3] K. Spindler, *The man in the ice: the discovery of a 5000 year-old body reveals the secrets of stone age* (Harmony Books, New York, 2006).

[4] T. Kamo, M. Asanoma, H. Shibata, and M. Hirota, Journal of natural products **66**, 1104 (2003).

[5] E. W. Hayek, U. Jordis, W. Moche, and F. Sauter, Phytochemistry **28**, 2229 (1989).

[6] Y. Hua, M. D. Bentley, B. J. W. Cole, K. D. Murray, and A. R. Alford, Journal of Wood Chemistry and Technology **11**, 503 (1991).

[7] G. M. Cragg and D. J. Newman, Plants as a source of anti-cancer agents, in *Ethnopharmacology, Encyclopedia of Life Support Systems*, edited by E. Elisabetsky and N. Etkin, Eolss, Oxford, 2004.

[8] P. A. Krasutsky, Natural Product Reports **23**, 919 (2006).

[9] S. Alakurtti, T. Mäkelä, S. Koskimies, and J. Yli-Kauhaluoma, European Journal of Pharmaceutical Sciences **29**, 1 (2006).

[10] S. Jäger, M. N. Laszczyk, and A. Scheffler, Molecules (Basel, Switzerland) **13**, 3224 (2008).

[11] J. Patočka, Journal of Applied Biomedicine **1**, 7 (2003).

[12] C. Gauthier *et al.*, Journal of Natural Products **72**, 72 (2009).

[13] A. Falamas, S. C. Pinzaru, V. Chis, and C. Dehelean, Journal of Molecular Structure **993**, 297 (2011).

[14] C. I. Peev, S. Ciurlea, R. Ambrus, and C. Dehelean, Farmacia **58**, 611 (2010).

[15] C. Peev, C. Dehelean, S. Feflea, and C. Tiulea, Studia Universitatis "Vasile Goldis" **20**, 41 (2010).

[16] G. Coneac *et al.*, Toxicology Letters **180**, S221 (2008).

[17] J. Szejtli, Chemical Reviews **98**, 1743 (1998).

[18] S. Shafiq *et al.*, European Journal of Pharmaceutics and Biopharmaceutics **66**, 227 (2007).

[19] S. Baboota, F. Shakeel, A. Ahuja, J. Ali, and S. Shafiq, Acta pharmaceutica (Zagreb, Croatia) **57**, 315 (2007).

[20] C. A. Dehelean, S. Feflea, S. Ganta, and M. Amiji, Journal of Biomedical Nanotechnology **7**, 317 (2011).

[21] P. Shah, D. Bhalodia, and P. Shelat, Systematic Reviews in Pharmacy **1**, 24 (2010).

[22] C. I. Peev, C. A. Dehelean, C. M. Soica, G. H. Coneac, and A. T. Gruia, Toxicology Letters **180**, S100 (2008).

[23] C. Tiulea *et al.*, Studia Universitatis "Vasile Goldis" **20**, 21 (2010).

[24] C. A. Dehelean, C. M. Soica, and C.-C. Toma, Studia Universitatis "Vasile Goldis" **20**, 55 (2010).

[25] J. Szejtli, Pure Appl Chem. **76**, 1825 (2004).

[26] T. Iliescu, M. Baia, and V. Miclaus, European journal of pharmaceutical sciences : official journal of the European Federation for Pharmaceutical Sciences **22**, 487 (2004).

[27] S. B. Tiwari and M. M. Amiji, Journal of Nanoscience and Nanotechnology **6**, 3215 (2006).

[28] G. Srinivas, D. Harikrishna, B. Bruce, G. Sanjay, and A. Mansoor, Journal of Biomedical Nanotechnology **4**, 165 (2008).

[29] F. Marchesi *et al.*, Pharmacological Research : The Official Journal of the Italian Pharmacological Society **56**, 275 (2007).

[30] A. M. M. Eggermont and J. M. Kirkwood, European journal of cancer (Oxford, England : 1990) **40**, 1825 (2004).

[31] P. B. Chapman *et al.*, J. Clin. Oncol. **17**, 2745 (1999).

[32] D. C. Lev *et al.*, Journal of clinical oncology : official journal of the American Society of Clinical Oncology **22**, 2092 (2004).

[33] M. Sanada, Y. Takagi, R. Ito, and M. Sekiguchi, DNA repair **3**, 413 (2004).

[34] J.-B. Tagne, S. Kakumanu, and R. J. Nicolosi, Molecular Pharmaceutics **5**, 1055 (2008).

[35] M. El Aatmani, S. Poujol, C. Astre, F. Malosse, and F. Pinguet, Official Journal of the American Society of Health-System Pharmacists **59**, 1351 (2002).

[36] B. V. Shetty, R. L. Schowen, M. Slavik, and C. M. Riley, Journal of Pharmaceutical and Biomedical Analysis **10**, 675 (1992).

[37] Y. Liu, W. Zhang, and Y. Yang, Talanta **77**, 412 (2008).

[38] O. Koreich and V. Shukla, Clinical Radiology **32**, 53 (1981).

[39] A. Szeghalmi *et al.*, Journal of Molecular Structure **735-736**, 103 (2005).

[40] N. Leopold *et al.*, Vibrational Spectroscopy **39**, 169 (2005).

[41] M. D. Keller, E. M. Kanter, and A. Mahadevan-Jansen, Spectroscopy **21**, 33 (2006).

[42] D. Dhawan, S. Balasubramanian, a. J. Amonkar, and N. Singh, Carcinogenesis **20**, 997 (1999).

[43] C. W. Boone, G. J. Kelloff, and W. E. Malone, Cancer Res. **50**, 2 (1990).

[44] P. J. Caspers, G. W. Lucassen, E. A. Carter, H. A. Bruining, and G. J. Puppels, The Journal of Investigative Dermatology **116**, 434 (2001).

[45] R. Aroca, *Surface Enhanced Vibrational Spectroscopy* (Wiley and Sons, West Sussex, UK, 2006).

[46] F. Bonnier *et al.*, Vibrational Spectroscopy **61**, 124 (2012).

[47] J. Kneipp, H. Kneipp, M. McLaughlin, D. Brown, and K. Kneipp, Nano Letters **6**, 2225 (2006).

[48] D. Ansari, *Raman-encoded nanoparticles for biomolecular detecion and cancer diagnosis*, PhD thesis, Georgia Institute of Technology, 2008.

[49] X.-M. Qian and S. M. Nie, Chemical Society Reviews **37**, 912 (2008).

[50] T. Vo-dinh, F. Yan, and M. B. Wabuyele, Surface-Enhanced Raman Scattering for Biomedical Diagnostics and Molecular, in *Surface-Enhanced Raman SCattering - Physics and Applications*, edited by K. Kneipp, M. Moskovits, and H. Kneipp Vol. 426, pp. 409–426, Berlin Heidleberg, , springer-v ed., 2006.

[51] T. Vo-Dinh, H.-N. Wang, and J. Scaffidi, Journal of Biophotonics **3**, 89 (2010).

[52] M. K. Gregas, F. Yan, J. Scaffidi, H.-N. Wang, and T. Vo-Dinh, Nanomedicine : nanotechnology, biology, and medicine **7**, 115 (2011).

[53] W. Xie, L. Su, A. Shen, A. Materny, and J. Hu, J. Raman Spectroscopy **42**, 1248 (2011).

[54] S. Schlücker, Chem. Phys. Chem. **10**, 1344 (2009).

[55] Katrin Kneipp *et al.*, Applied Spectroscopy **56**, 150 (2002).

[56] J. Kneipp, H. Kneipp, W. L. Rice, and K. Kneipp, Analytical chemistry **77**, 2381 (2005).

[57] K. Kneipp and H. Kneipp, Acc. Chem. Res. **39**, 443 (2006).

[58] Z. Movasaghi, S. Rehman, and I. Rehman, Applied spectroscopy **42**, 493 (2007).

[59] S. Fendel, B. Schrader, B. Fendel, and S. Schrader, Fresenius' Journal of Analytical Chemistry **360**, 609 (1998).

[60] H. Wang *et al.*, Journal of Raman Spectroscopy **42**, 160 (2011).

[61] A. Nijssen *et al.*, The Journal of investigative dermatology **119**, 64 (2002).

[62] N. Stone, P. Stavroulaki, C. Kendall, M. Birchall, and H. Barr, The Laryngoscope **110**, 1756 (2000).

[63] M. Gniadecka *et al.*, The Journal of investigative dermatology **122**, 443 (2004).

[64] X. Qian *et al.*, Nature Biotechnology **26**, 83 (2008).

[65] W. Doering, M. Piotti, M. Natan, and R. Freeman, Advanced Materials **19**, 3100 (2007).

[66] J. Creighton, No Title, in *Advances in Spectroscopy, vol.16*, edited by R. Clark and R. Hester, chap. 2, Wiley, New York, 1988.

[67] S. C. Pînzaru, L. M. Andronie, I. Domsa, O. Cozar, and S. Astilean, Journal of Raman Spectroscopy **39**, 331 (2008).

[68] J. Kneipp, H. Kneipp, B. Wittig, and K. Kneipp, Nanomedicine : Nanotechnology, Biology, and Medicine **6**, 214 (2010).

[69] C. Otto, T. van den Tweel, F. de Mul, and J. Greve, J. Raman Spectroscopy **17**, 289 (1986).

[70] O. Aydin, M. Altas, M. Kahraman, O. F. Bayrak, and M. Culha, Applied Spectroscopy **63**, 1095 (2009).

[71] A. Barhoumi, D. Zhang, F. Tam, and N. J. Halas, Journal of the American Chemical Society **130**, 5523 (2008).

[72] Z. Huang, Z. Li, R. Chen, G. Chen, and D. Lin, J. Physics: Conference Series **277**, 012014 (2011).

[73] J. W. Chan and D. K. Lieu, Journal of biophotonics **2**, 656 (2009).

[74] A. Downes, R. Mouras, and A. Elfick, Journal of Biomedicine & Biotechnology **2010**, 101864 (2010).

[75] I. Notingher and L. Hench, Expert Rev. Med. Devices **3**, 215 (2006).

[76] C. A. Cowan *et al.*, The New England Journal of Medicine **350**, 1353 (2004).

[77] E. Zuser, T. Chernenko, J. Newmark, M. Miljković, and M. Diem, The Analyst **135**, 3030 (2010).

[78] C. Matthäus *et al.*, Proc. of SPIE **6991**, 699106 (2008).

[79] H. G. Schulze *et al.*, Analytical chemistry **82**, 5020 (2010).

[80] F. Bonnier *et al.*, The Analyst **135**, 3169 (2010).

[81] I. Notingher *et al.*, Analytical chemistry **76**, 3185 (2004).

[82] I. Notingher, I. Bisson, J. M. Polak, and L. L. Hench, Vibrational Spectroscopy **35**, 199 (2004).

[83] A. Ghita, F. C. Pascut, M. Mather, V. Sottile, and I. Notingher, Analytical chemistry **84**, 3155 (2012).

[84] I. Notingher, Sensors **7**, 1343 (2007).

[85] K. W. Short, S. Carpenter, J. P. Freyer, and J. R. Mourant, Biophysical journal **88**, 4274 (2005).

[86] S. O. Konorov *et al.*, Analytical chemistry **83**, 6254 (2011).